Electronic Supplementary Information for:

Inherently chiral cone-calix[4]arenes via a subsequent upper rim ring-closing/opening methodology

José Augusto Berrocal,[a]* Matthew B. Baker,[b] Laura Baldini,[c] Alessandro Casnati,[c] Stefano Di Stefano[d]

[a] Institute for Complex Molecular Systems and Laboratory of Macromolecular and Organic Chemistry, Eindhoven University of Technology, 5600 MB Eindhoven, the Netherlands.

[b] MERLN Institute for Technology-Inspired Regenerative Medicine, Maastricht University, 6200 MD Maastricht, the Netherlands.

[c] Dipartimento di Chimica, Università degli Studi di Parma, Parco Area delle Scienze 17/A, 43124 Parma, Italy.

[d] Dipartimento di Chimica and IMC – CNR Sezione Meccanismi di Reazione, Università La Sapienza, 00185 Roma, Italy.

* To whom correspondence should be addressed:

jaberroc@gmail.com

Table of contents

Conformational motions of *cone* calix[4]arenes

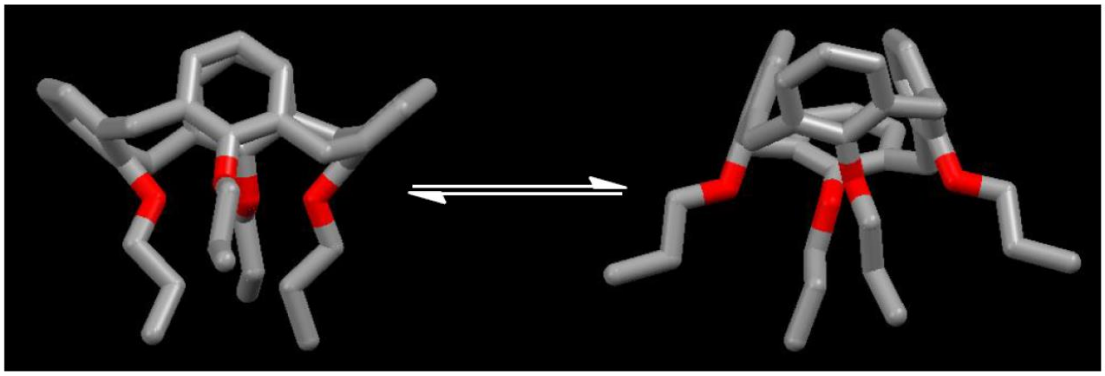

Figure S1. Major conformational motions of *cone* calix[4]arenes

Spectroscopic Characterization.

Lactones **1–3** were characterized with Fourier-Transform Infrared (FT-IR) spectroscopy, ^{1}H- and ^{13}C-NMR spectroscopy, Ultraviolet-Visible (UV-Vis) spectroscopy and either Matrix Assisted Laser Desorption Ionization-Time Of Flight or Electrospray Ionization-Time Of Flight mass spectrometry (MALDI-TOF-MS and ESI-TOF-MS, respectively).

A close comparison between the FT-IR spectra of lactones **1–3** and their corresponding precursors **4–6** qualitatively shows considerable differences in the carbonyl stretching frequencies. Lactones **1–3** generally possess more intense and narrow carbonyl peaks compared to their open precursors in the solid state (ESI, Figures S30-S34).

Three distinct regions can be observed in the ^{1}H-NMR spectrum ($CDCl_3$, 400 MHz) of the calix[4]arenes derivatives, namely the aromatic (8.0–6.0 ppm range) and aliphatic (5.0–3.0 ppm) protons, and the terminal methyl groups of the -$OCH_2CH_2OCH_2CH_3$ chains at the lower rim (1.5–1.0 ppm, Figure S2). Shifts and splitting of selected signals are clearly visible after cyclization of **4** into **1** (Figure S2 and Figure S17). The singlets at 7.1 and 6.4 ppm in the ^{1}H-NMR spectrum of **4** (Figure S2, brown trace) are shifted upfield to 6.2 and 6.1 ppm in **1** (Figure S2, green trace), while the rest of the aromatic signals move to lower fields. The diagnostic signal of **1** is the sharp singlet of the benzylic methylene group at 4.7 ppm (Figure S2, green trace). This peak is significantly deshielded with respect to its hydroxymethyl counterpart in **4**, which resonates at 4.2 ppm (Figure S2, brown trace, denoted with a star). All of these general trends are well reproduced via calculation of the NMR shifts (*vide infra*) of the minimized structures. Additional consequences of the **4** → **1** ring closure are visible in the rest of the signals of the aliphatic and terminal methyl groups. A clearer splitting of the methyl signal into three triplets with ratio 1:1:2 is observed for lactone **1** (Figure S2, green trace) with respect to the open parent **4** (Figure S2, brown trace). However, both **4** and **1** possess a symmetry plane which confers the same multiplicity to the related ^{1}H NMR signals.

Further complexity appears in the ^{1}H-NMR spectra upon introducing the third chemical functionality at the upper rim of the lactones, as in **2** and **3** (Figure S2, cyan and purple traces, respectively). The resultant symmetry break is particularly visible in the aromatic region through the splitting of the singlets in the 6.4–6.0 ppm range and

emergence of new signals at 7.8 and 8.0 for **2** and **3**, respectively. The latter change is associated to the protons *ortho* to the formyl (**2**) or carboxy (**3**) groups. More remarkably, the symmetry break confers significant differences in terms of chemical shifts to the benzylic methylene protons of the lactone moieties. The diagnostic singlet of **1** at 4.7 ppm becomes an AB system in **2** and **3**. It should be underlined that the diastereomeric character of the benzylic methylene protons is also a feature of **5** and **6**, but they lack the significant distinction in chemical shifts (Figures S18 and S19) observed for compounds **2** and **3**. We ascribe such behavior to the formation of the rigid intramolecular lactone bond. Lastly, spectral differences are also observed in the region of the terminal methyl groups, with the more intense triplet of **1** (1.2 ppm; Figure S2, green trace) that splits into two new triplets in **2** and **3** (Figure S2, cyan and purple traces).

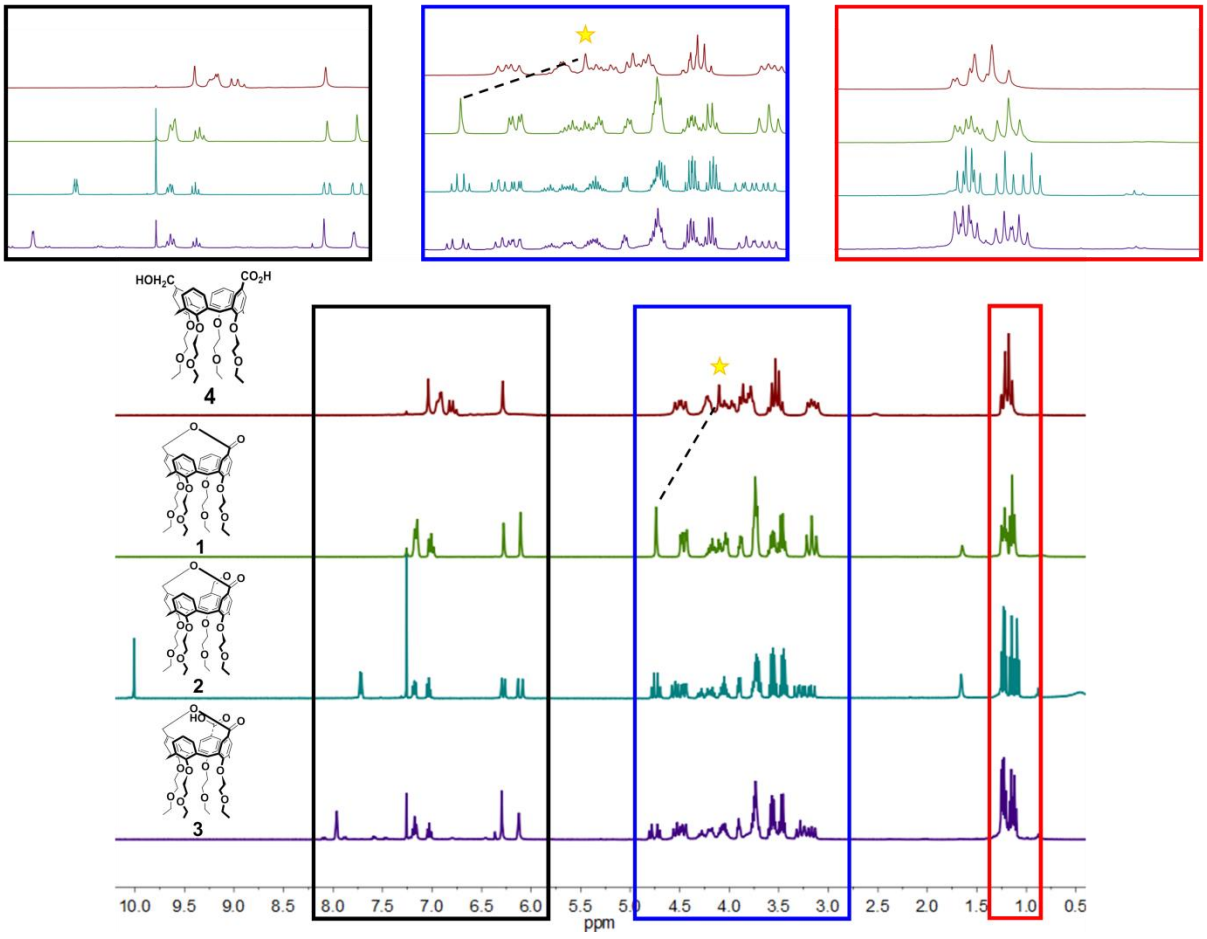

Figure S2. ^{1}H-NMR spectra ($CDCl_3$, 400 MHz) of **4** (brown trace), **1** (green trace), **2** (cyan trace) and **3** (purple trace). The insets (colored boxes) show the expansions of the aromatic (black box), aliphatic (blue box) and terminal methyl groups (red box) regions of the ^{1}H NMR spectra

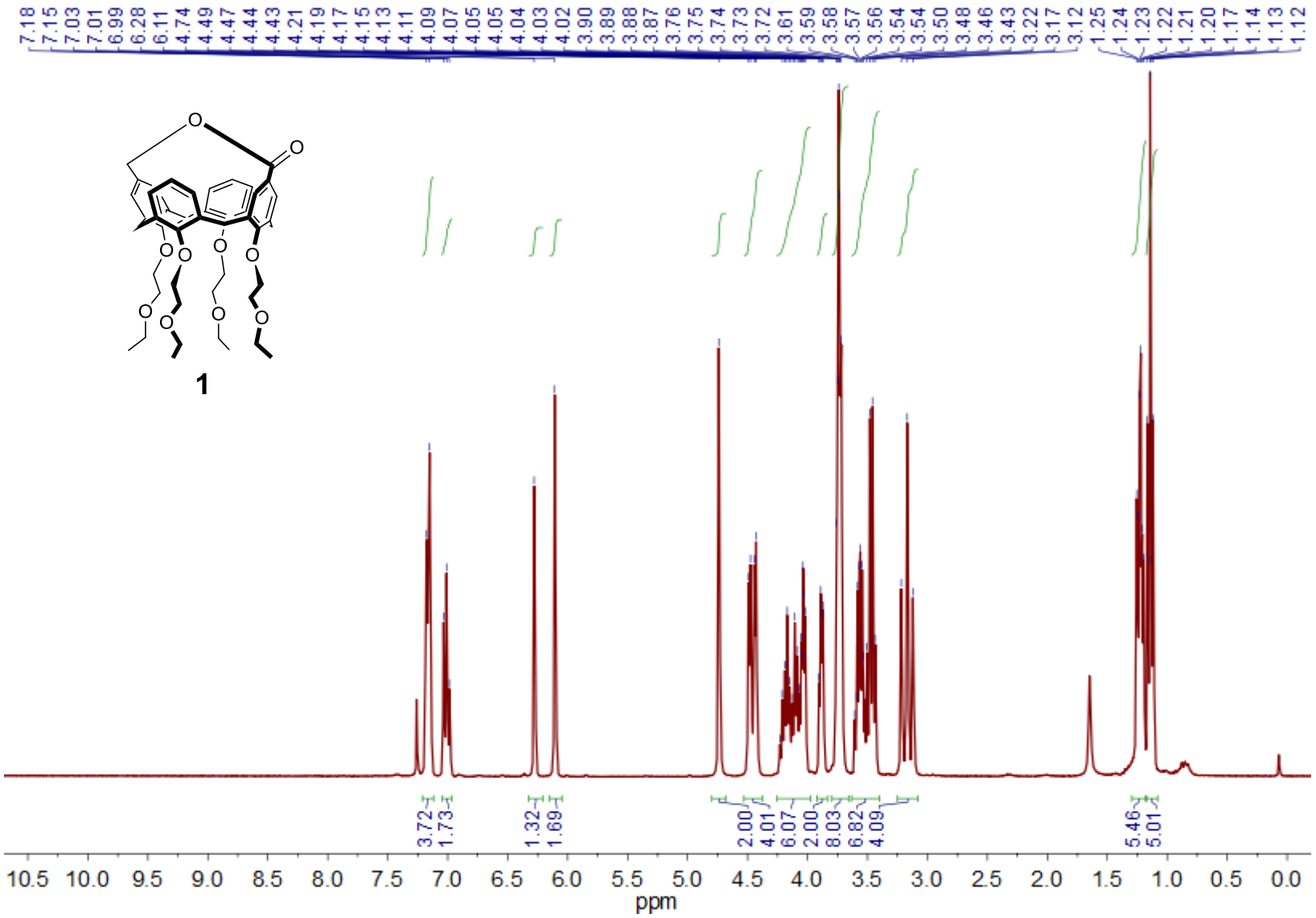

Figure S3. ^{1}H NMR spectrum of lactone **1** (300 MHz, $CDCl_3$).

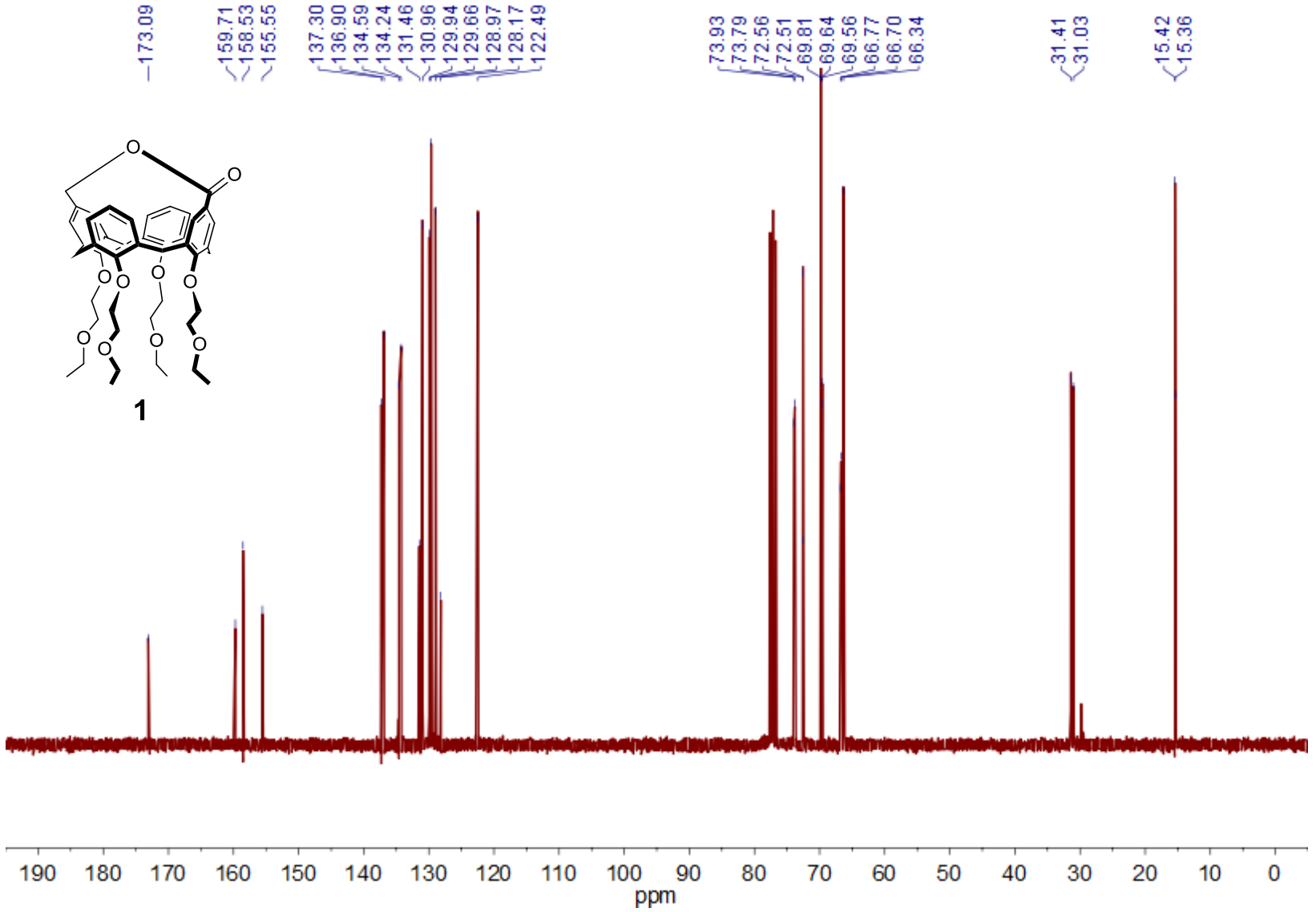

Figure S4. ^{13}C NMR spectrum of lactone **1** (75 MHz, $CDCl_3$).

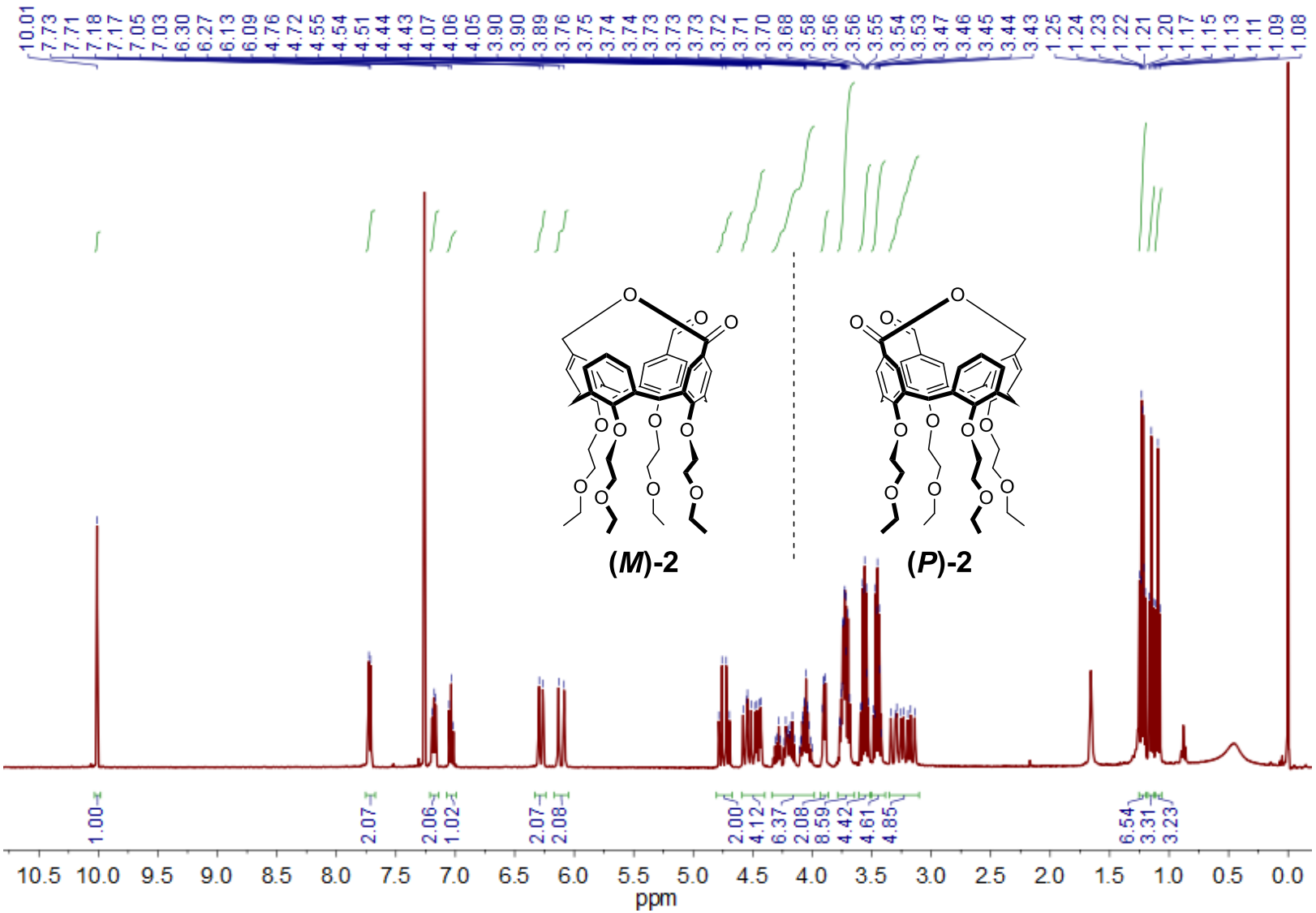

Figure S5. ^{1}H NMR spectrum of lactone **2** (400 MHz, $CDCl_3$).

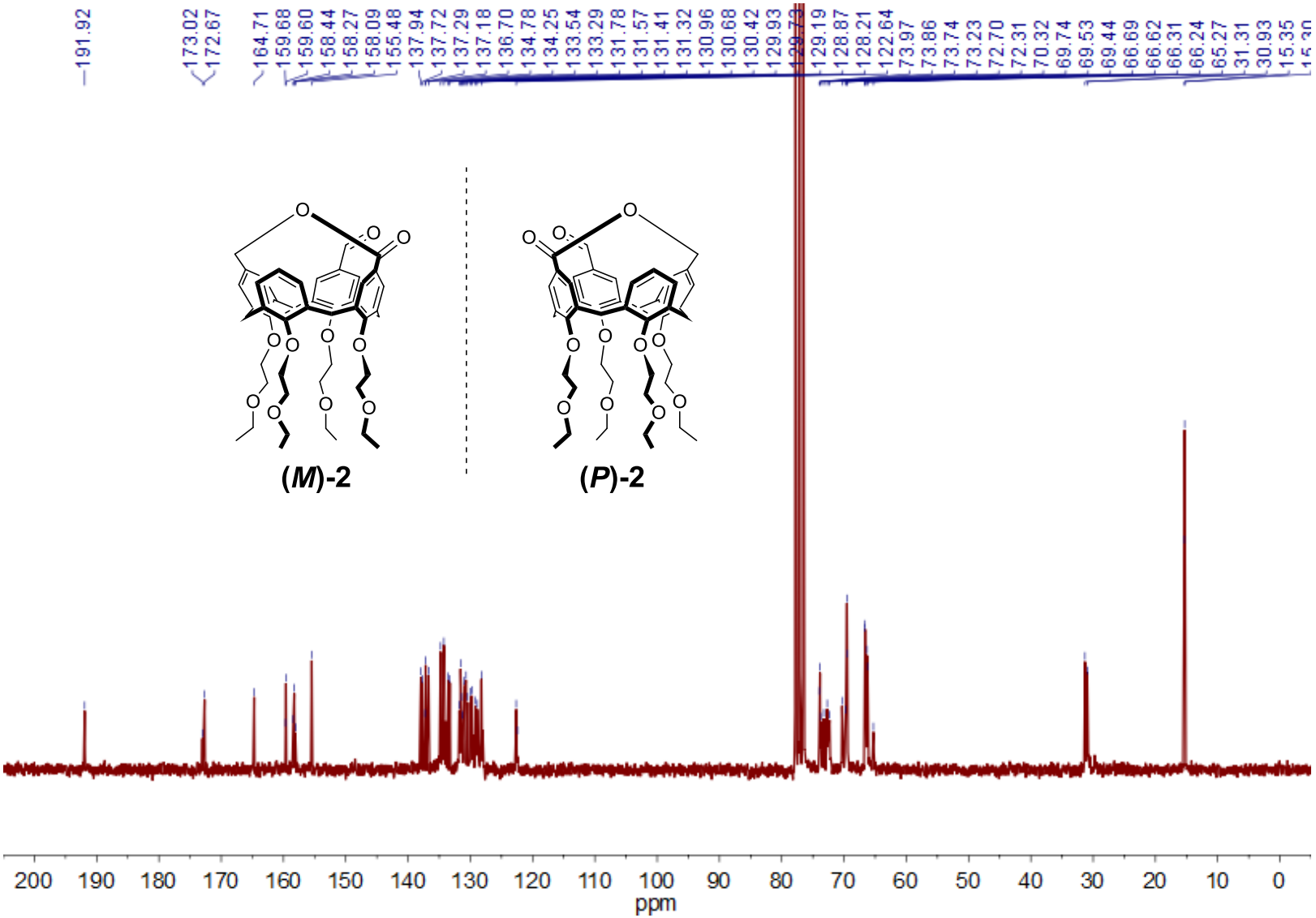

Figure S6. ^{13}C NMR spectrum of lactone **2** (100 MHz, $CDCl_3$).

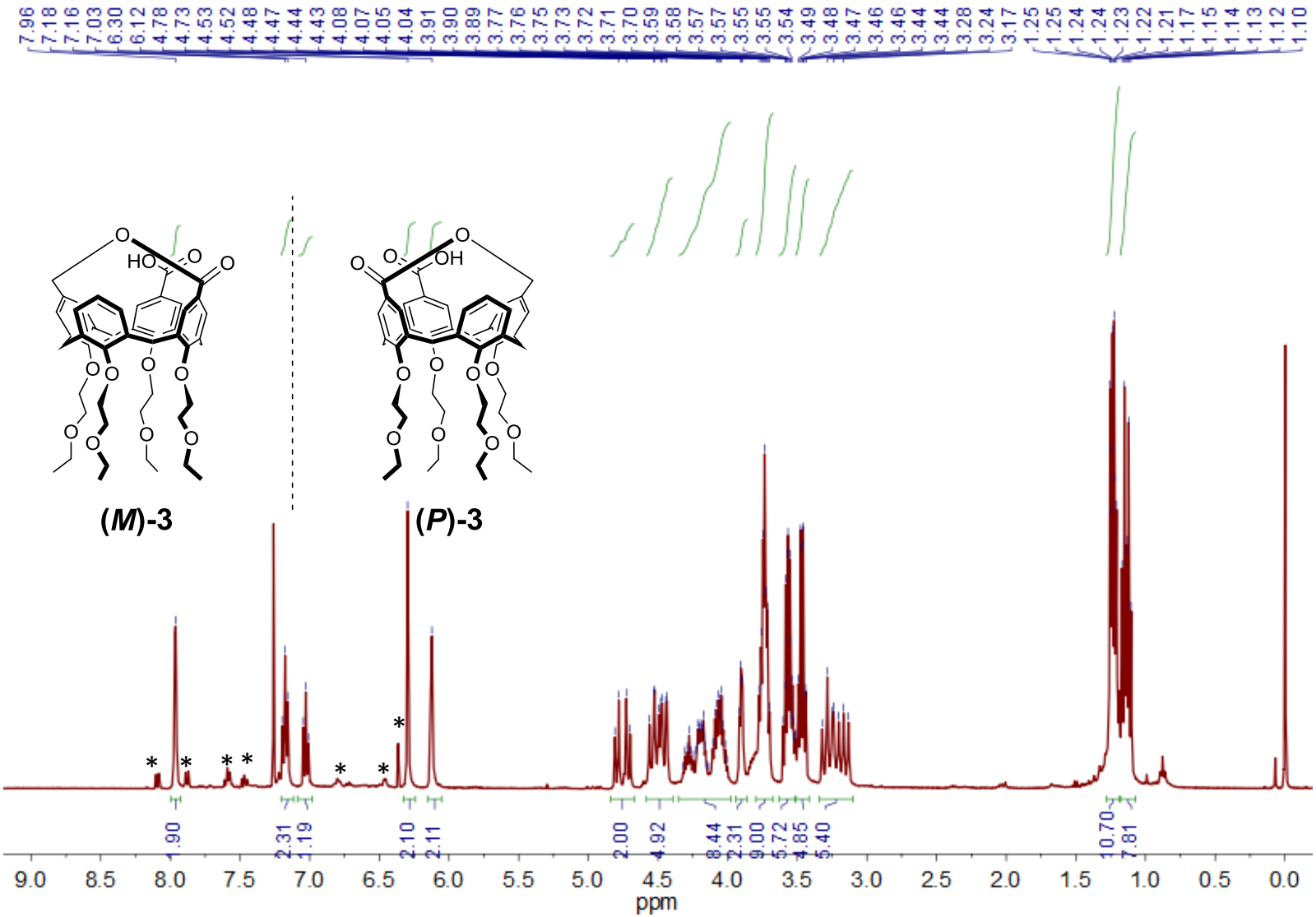

Figure S7. ^{1}H NMR spectrum of lactone **3** (400 MHz, $CDCl_3$). The signals marked with an asterisk are related to ring-opened precursor **6** and additional minor impurities.

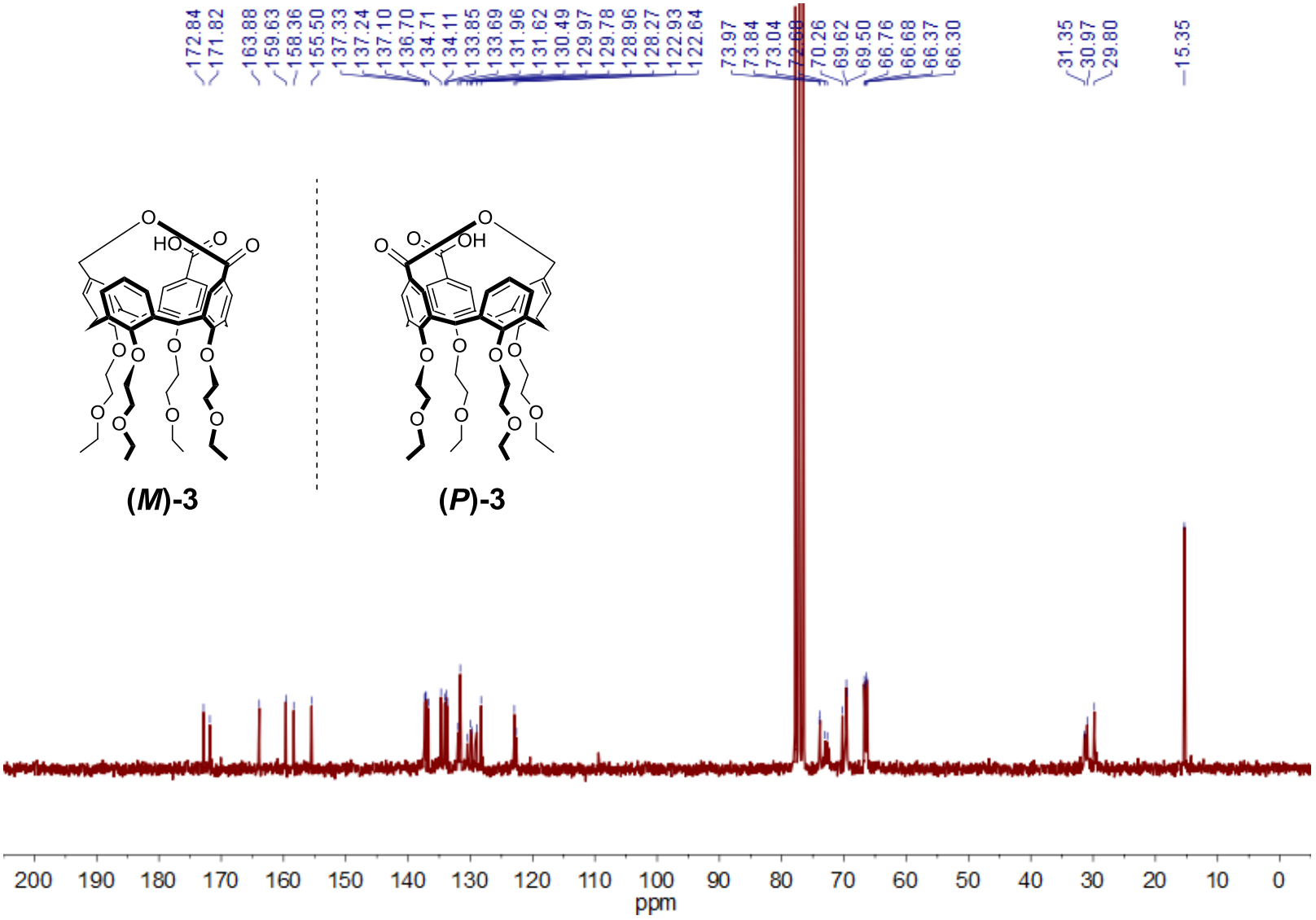

Figure S8. ^{13}C NMR spectrum of lactone **3** (100 MHz, $CDCl_3$).

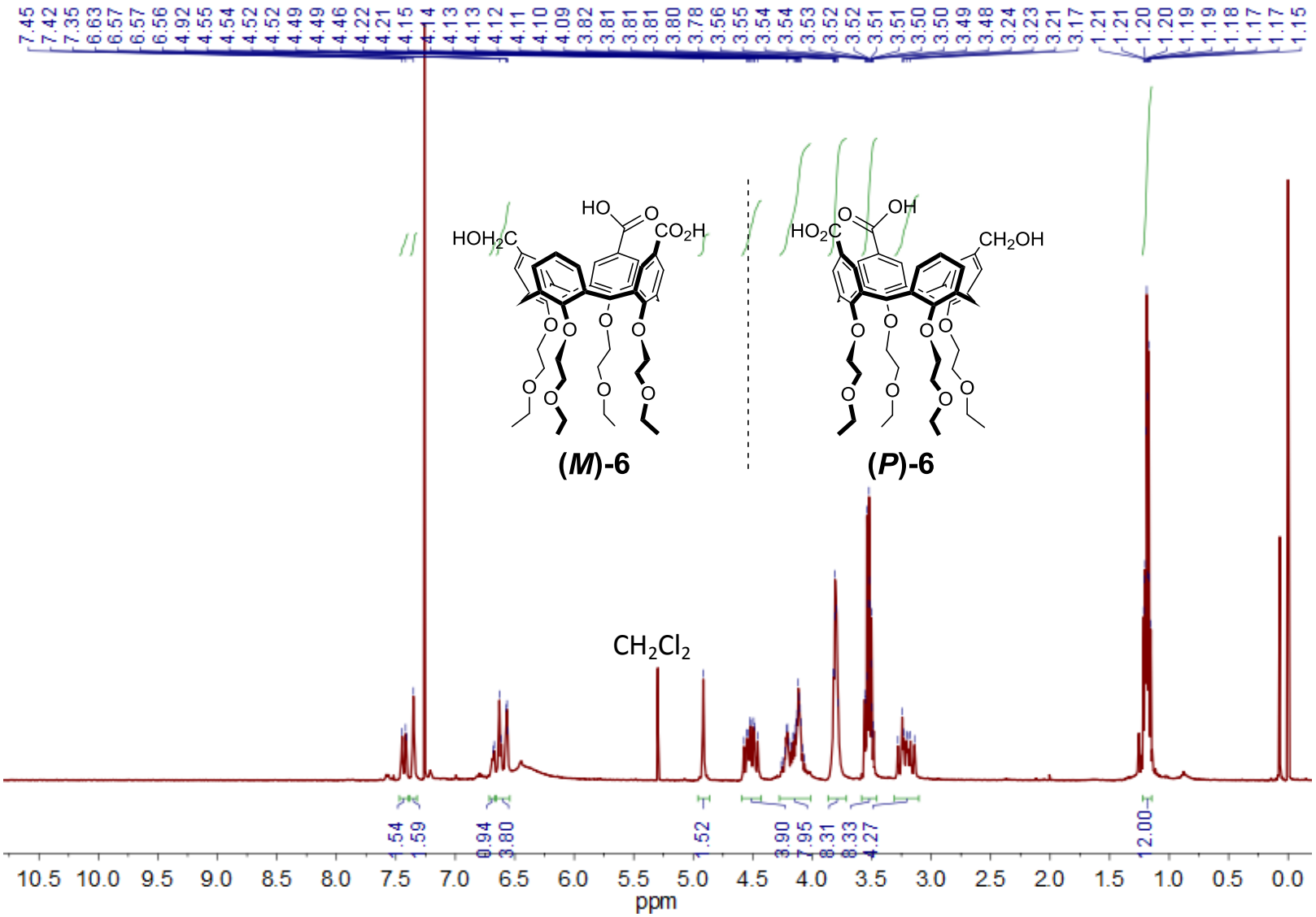

Figure S9. ^{1}H NMR spectrum of compound **6** (400 MHz, $CDCl_3$).

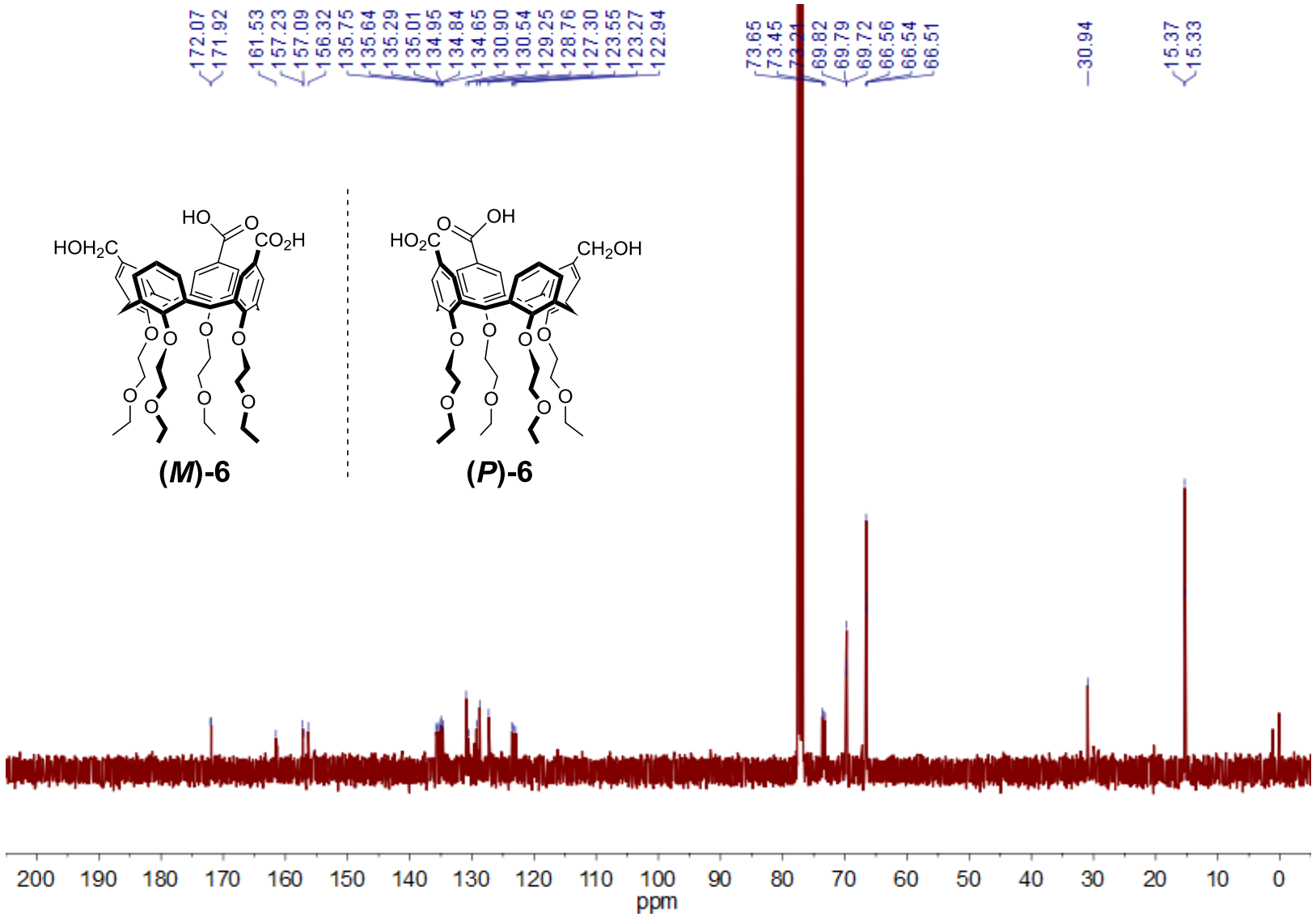

Figure S10. ^{13}C NMR spectrum of compound **6** (100 MHz, $CDCl_3$).

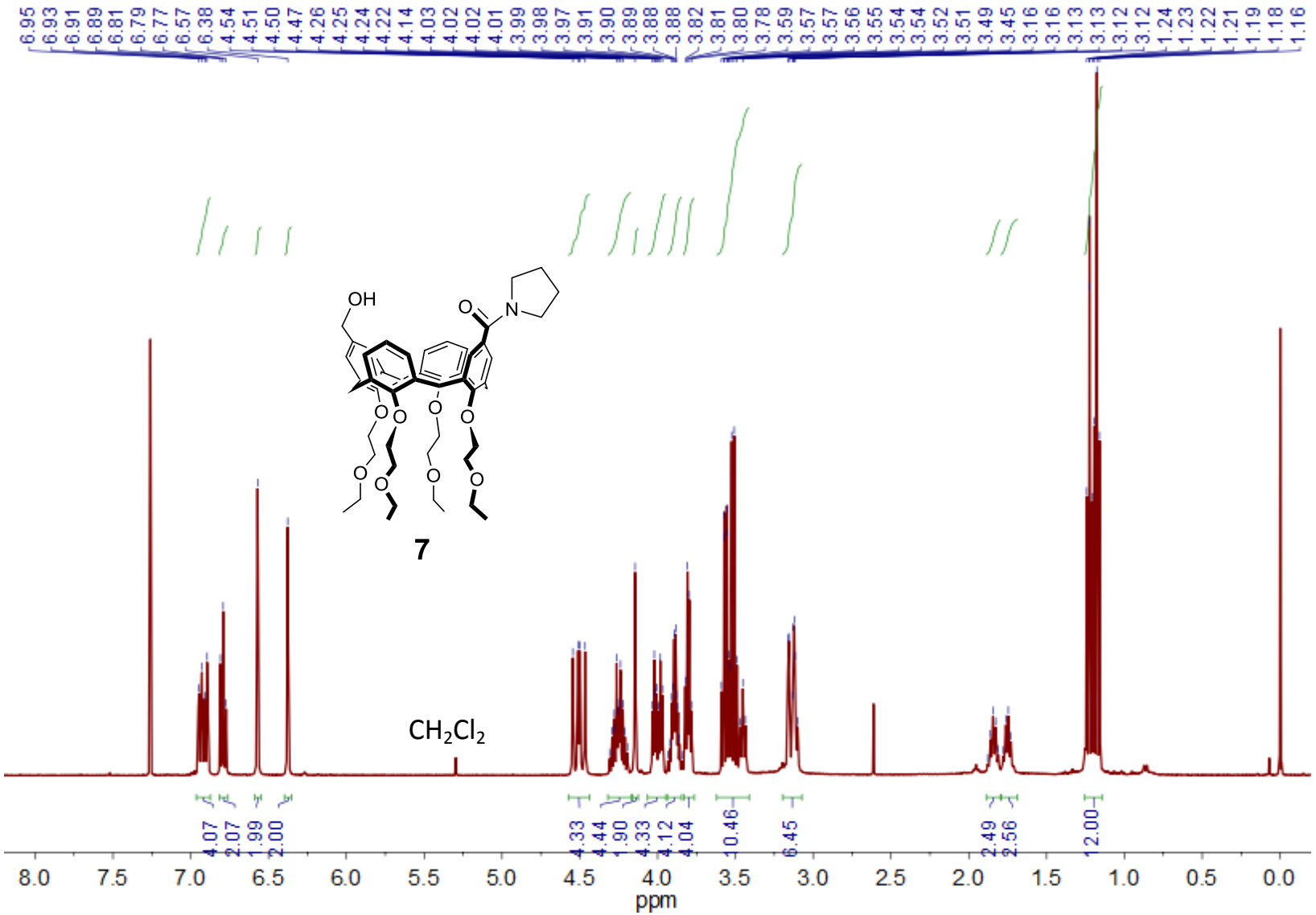

Figure S11. ^{1}H NMR spectrum of compound **7** (400 MHz, $CDCl_3$).

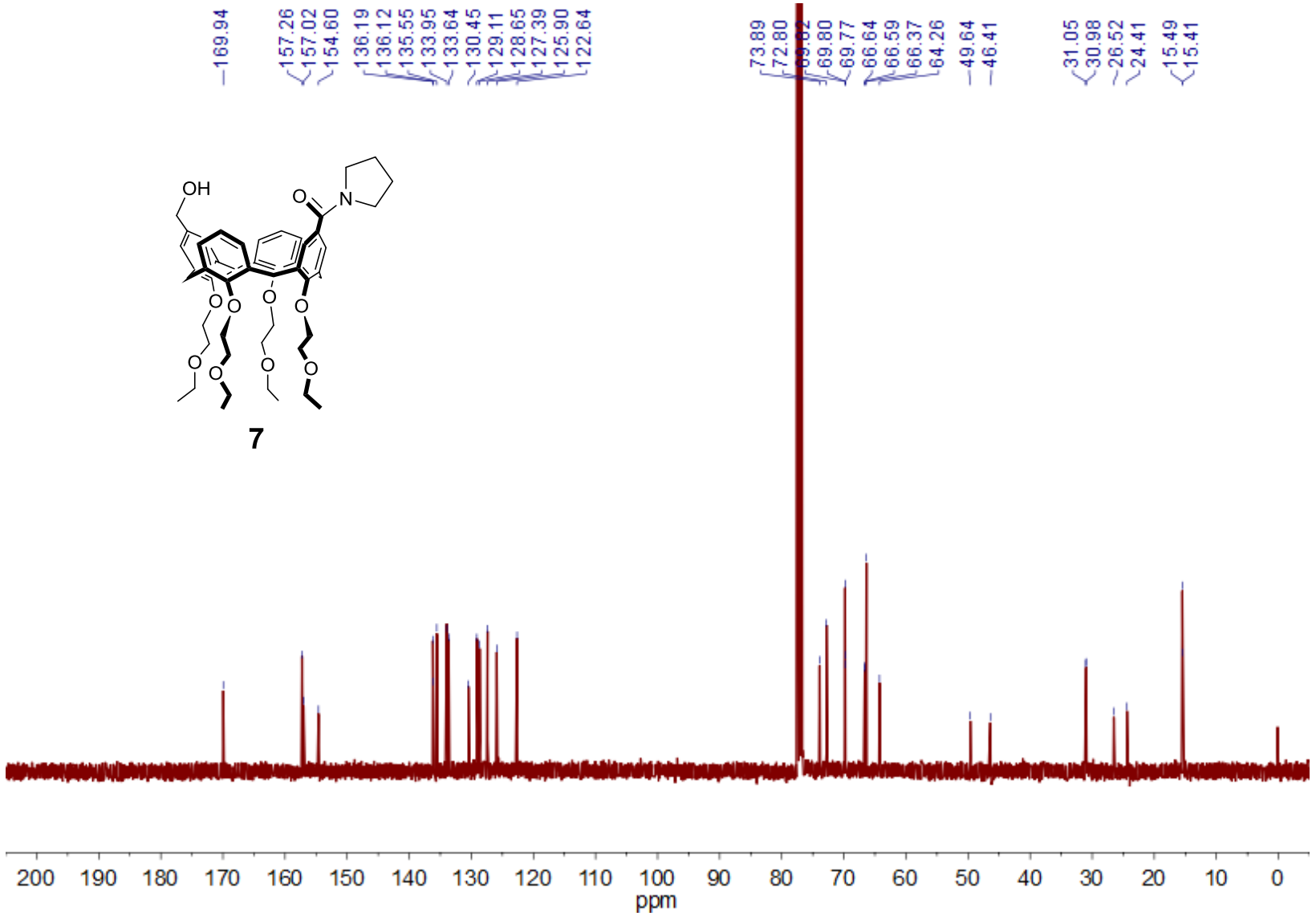

Figure S12. ^{13}C NMR spectrum of compound **7** (100 MHz, $CDCl_3$).

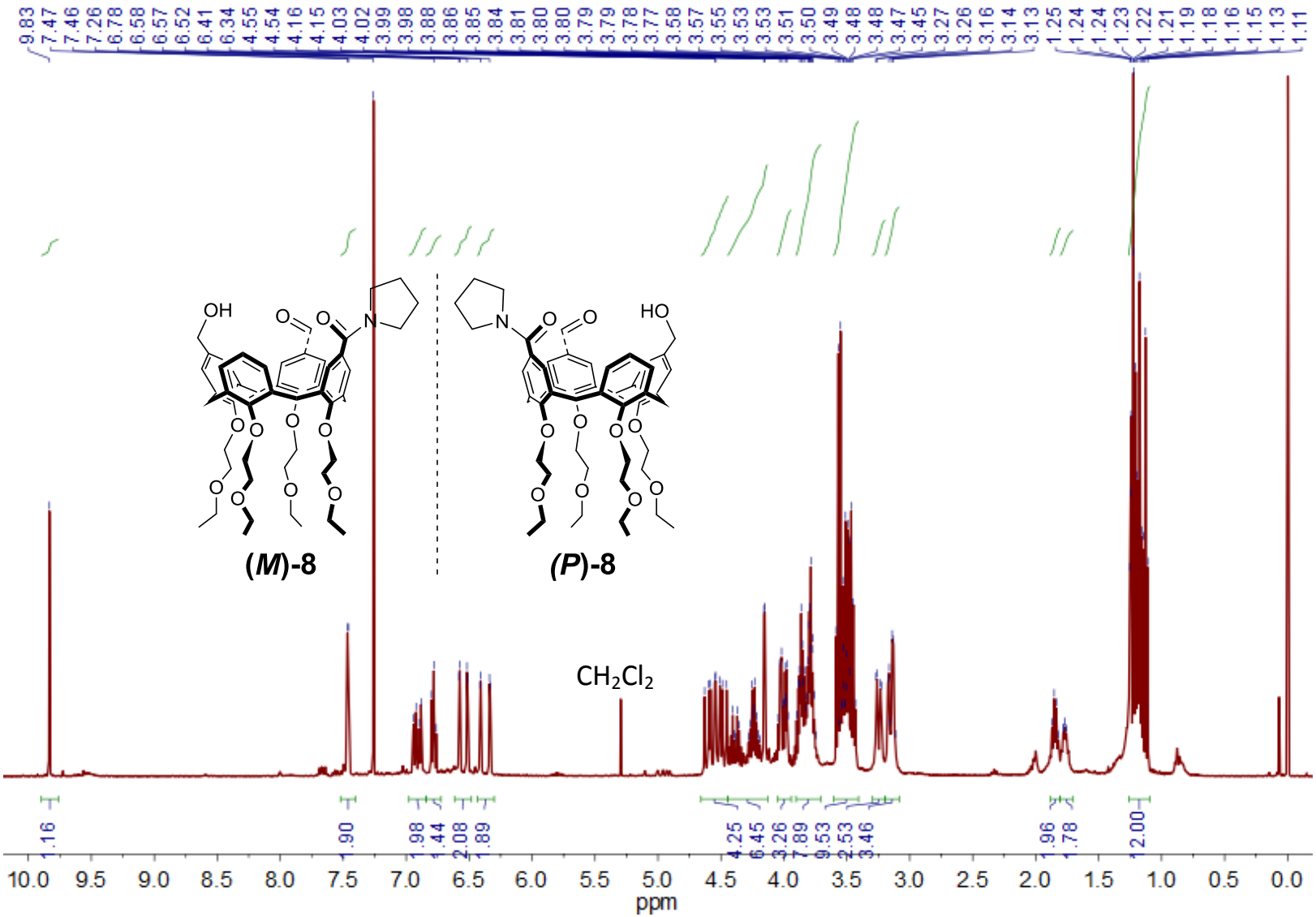

Figure S13. ^{1}H NMR spectrum of compound **8** (400 MHz, $CDCl_3$).

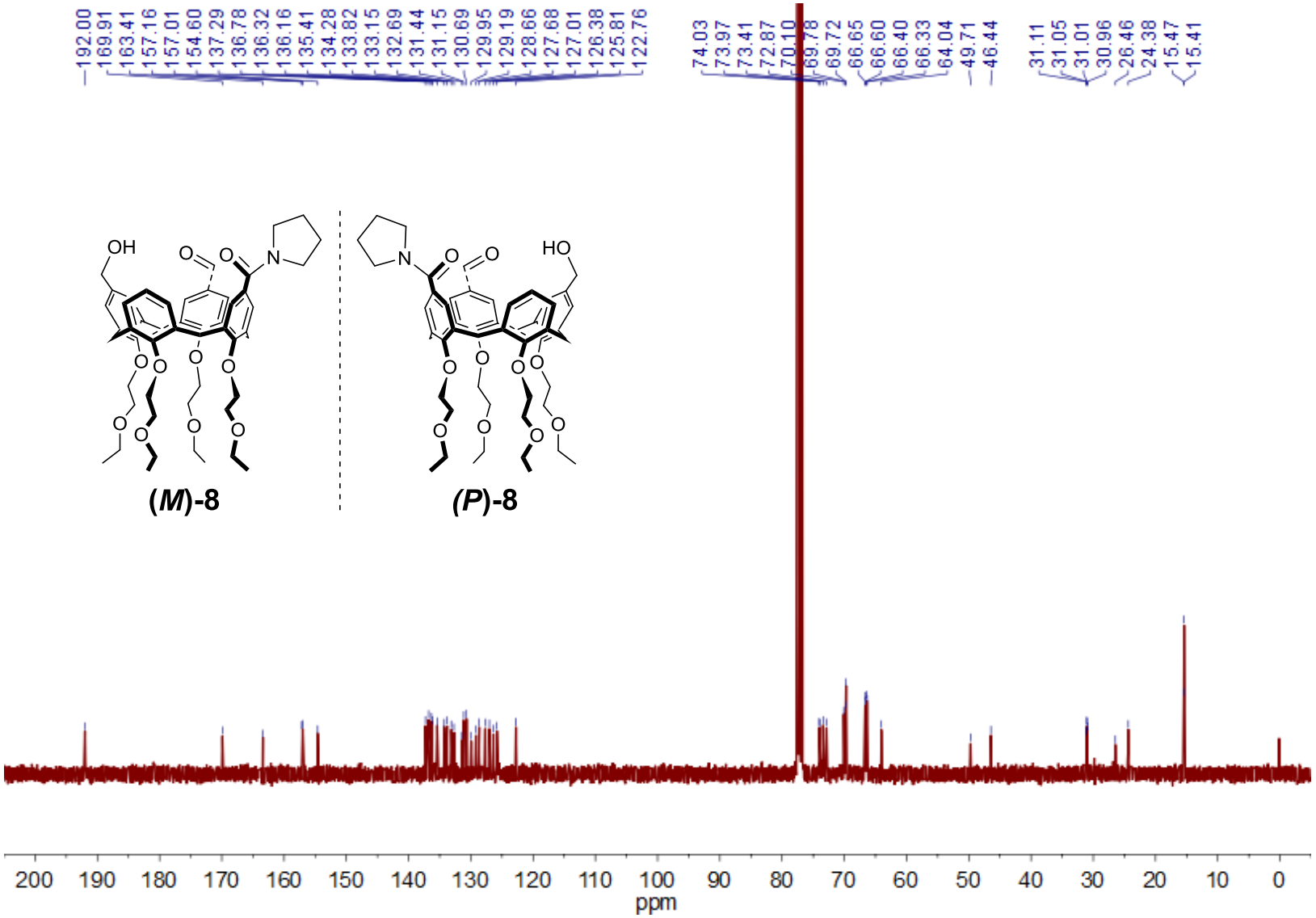

Figure S14. ^{13}C NMR spectrum of compound **8** (100 MHz, $CDCl_3$).

^{1}H NMR spectra comparisons

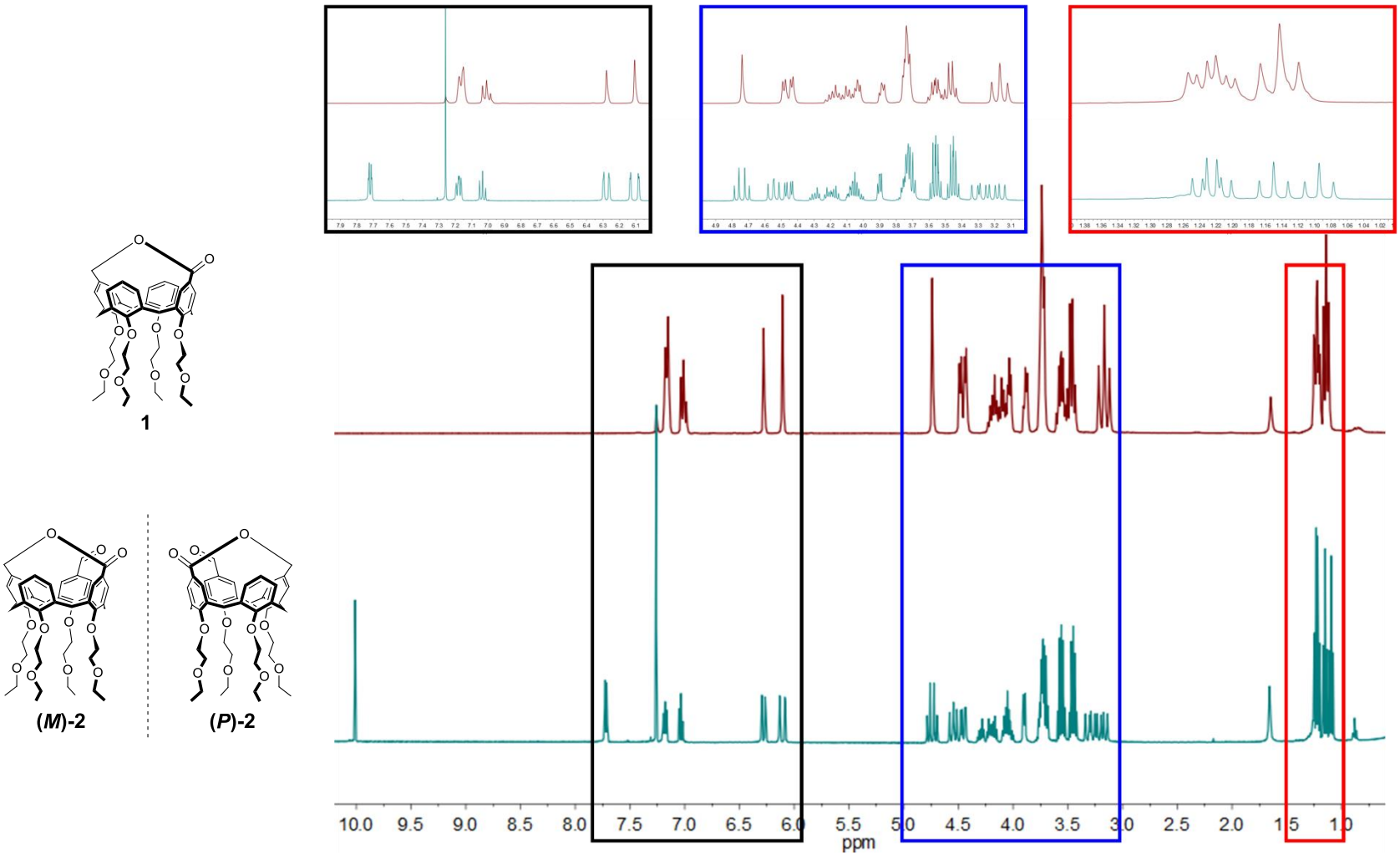

Figure S15. Comparison of ^{1}H NMR spectra of **1** and **2**.

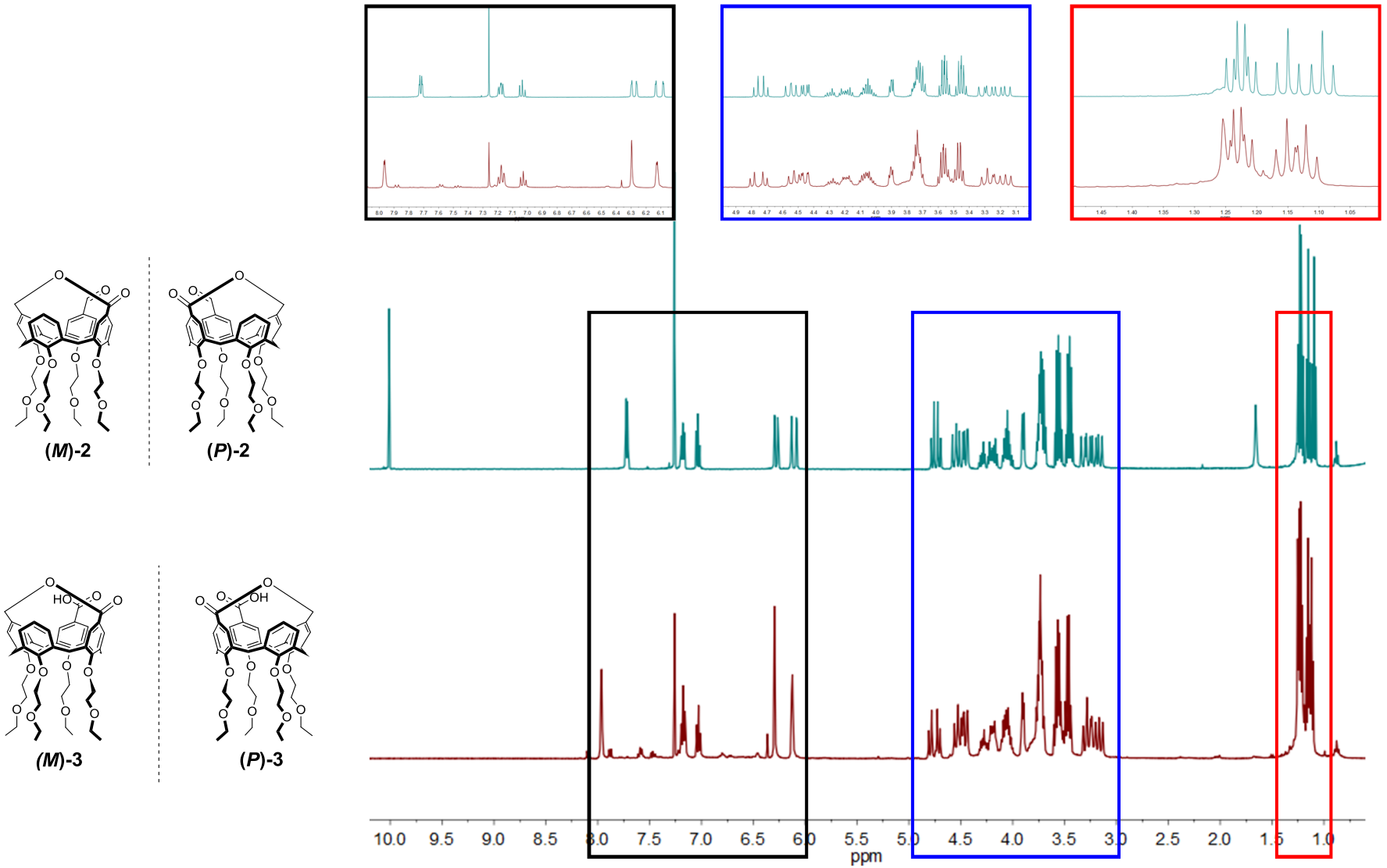

Figure S16. Comparison of ^{1}H NMR spectra of **2** and **3**.

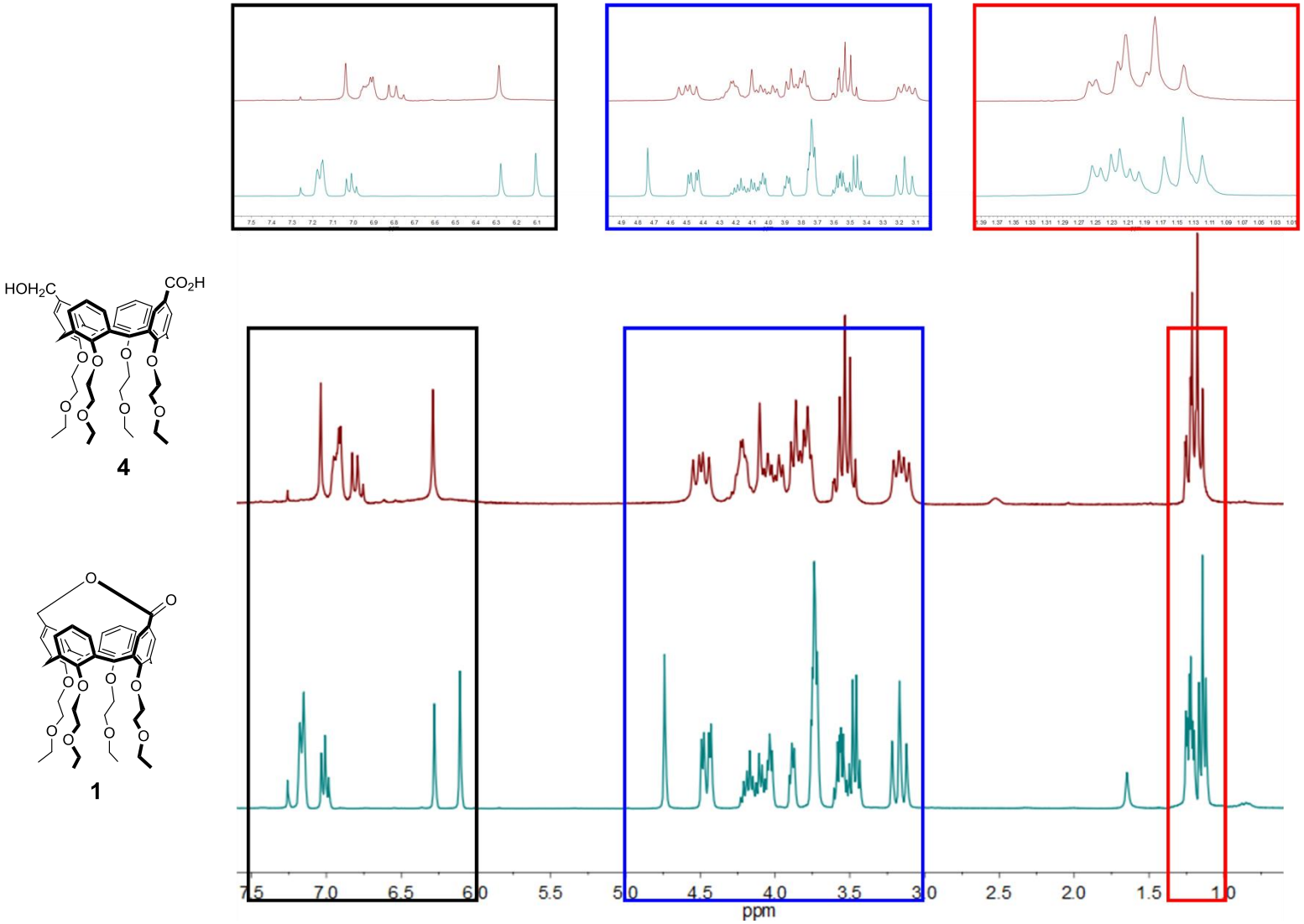

Figure S17. Comparison of ^{1}H NMR spectra of **1** and its precursor **4**.

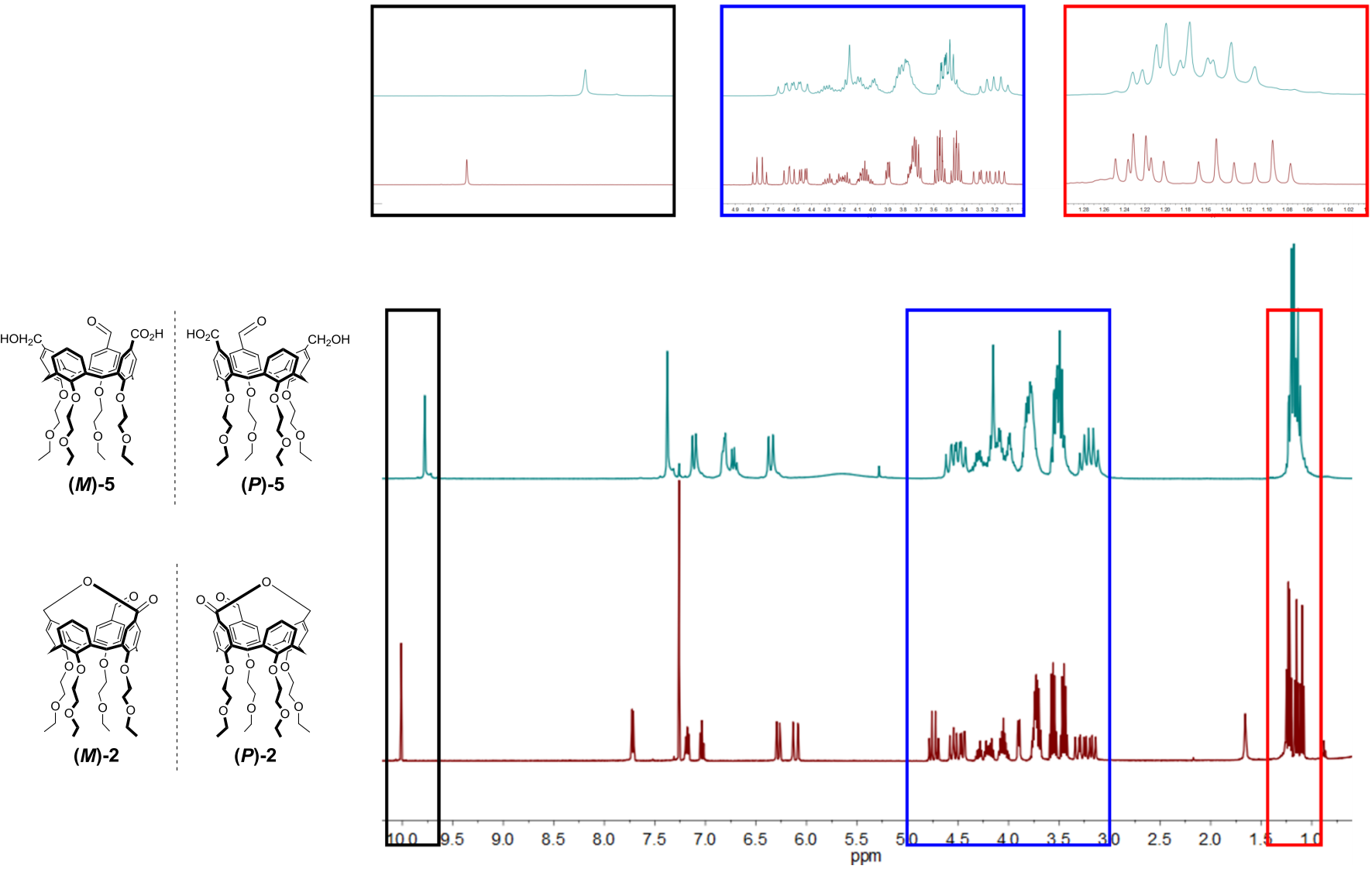

Figure S18. Comparison of ^{1}H NMR spectra of **2** and its precursor **5**.

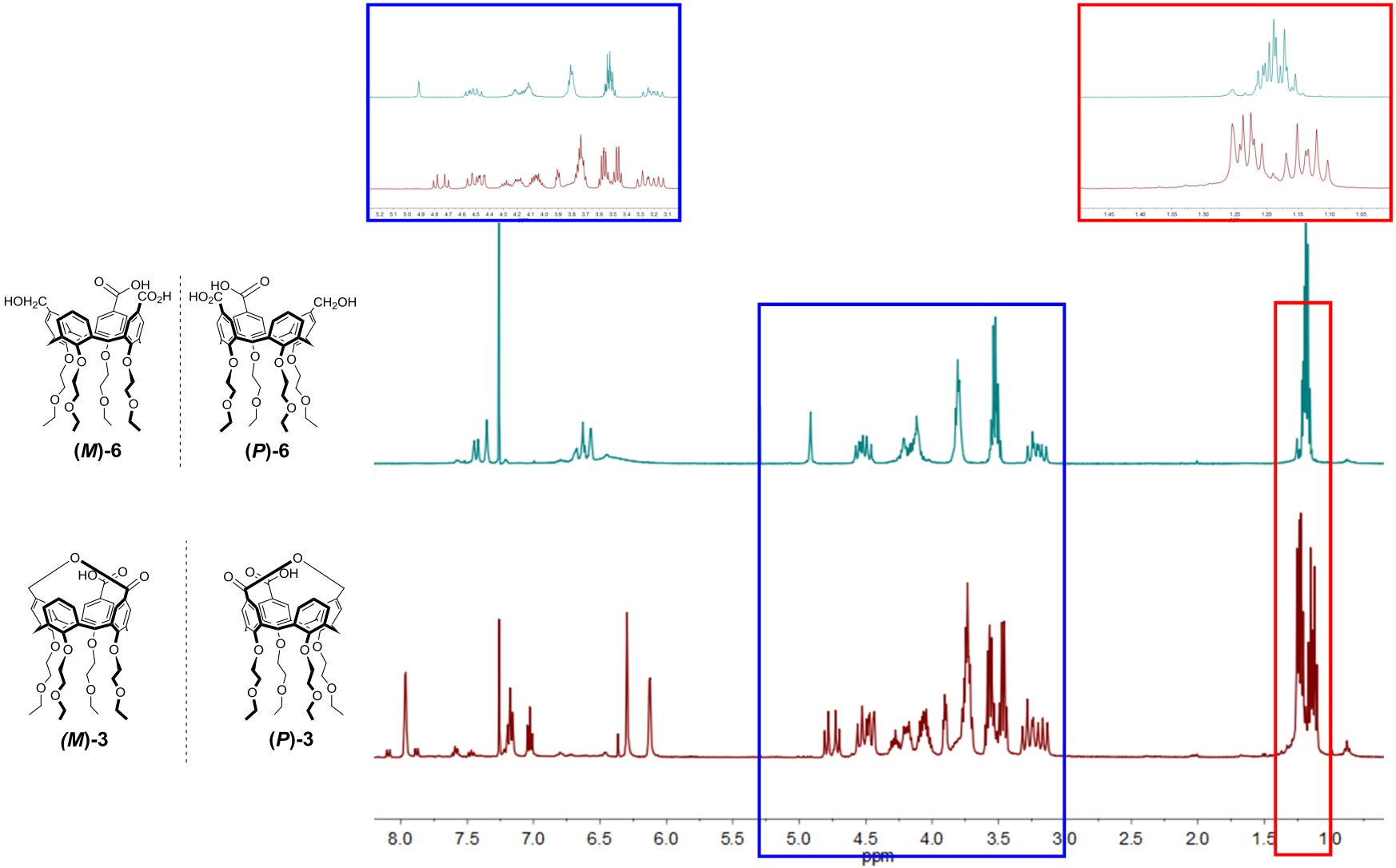

Figure S19. Comparison of ^{1}H NMR spectra of **3** and its precursor **6**.

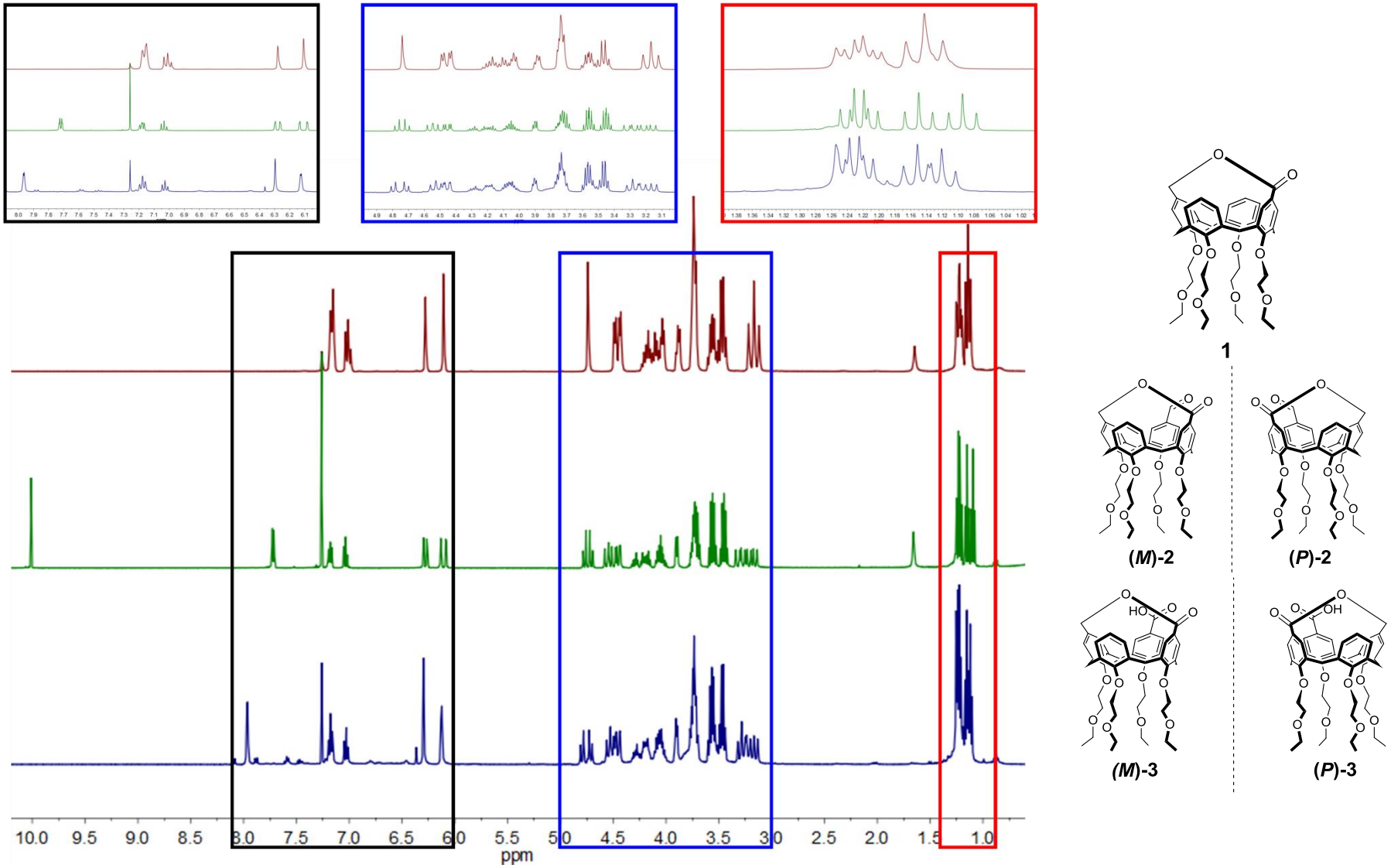

Figure S20. Comparison of ^{1}H NMR spectra of lactones **1**, **2** and **3**.

Stability of racemic lactone 2 in untreated $CDCl_3$ (<u>not</u> flushed through basic alumina)

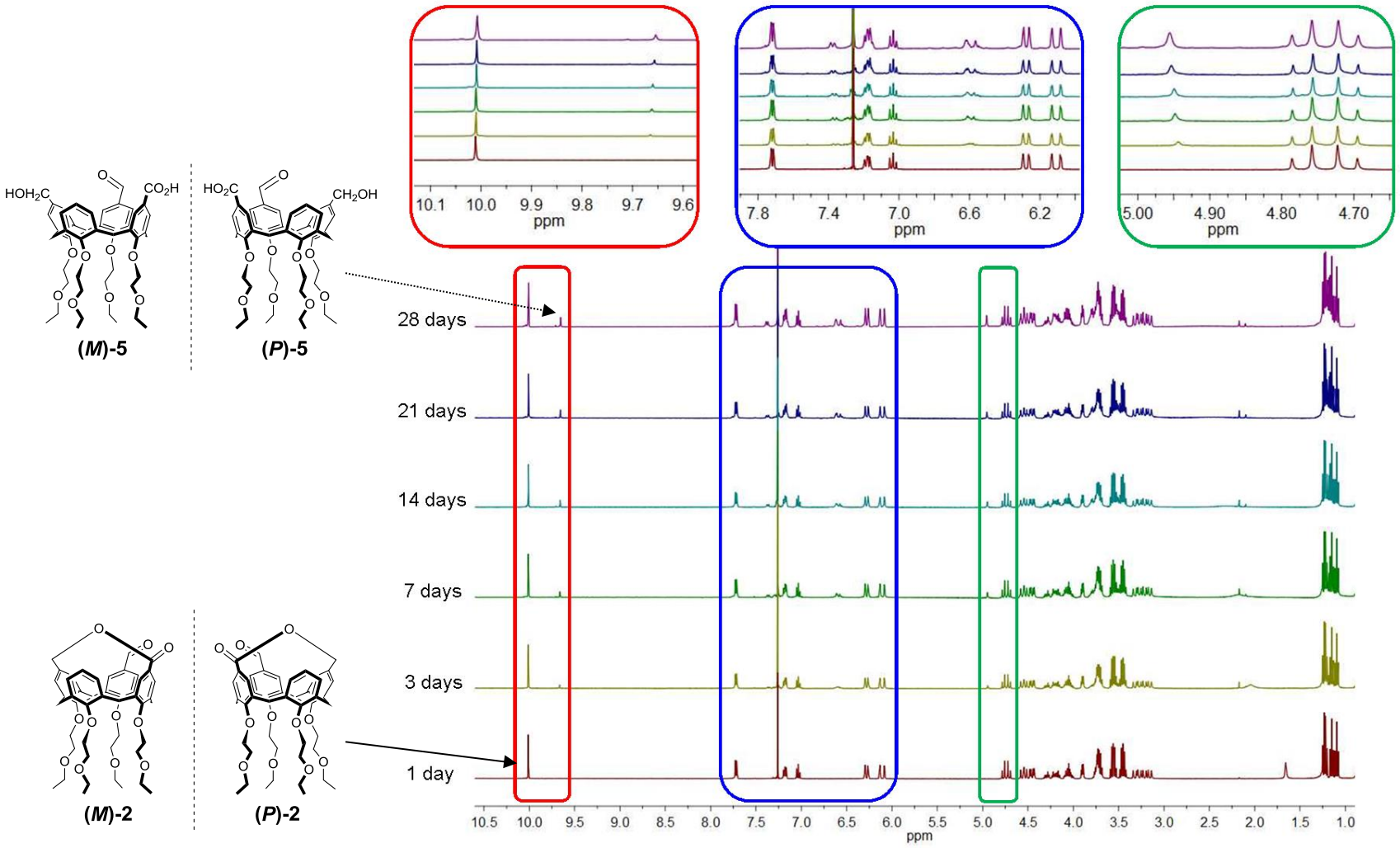

Figure S21. ^{1}H NMR spectra of lactones **2** in untreated $CDCl_3$ measured over a period of 28 days.

IR spectra

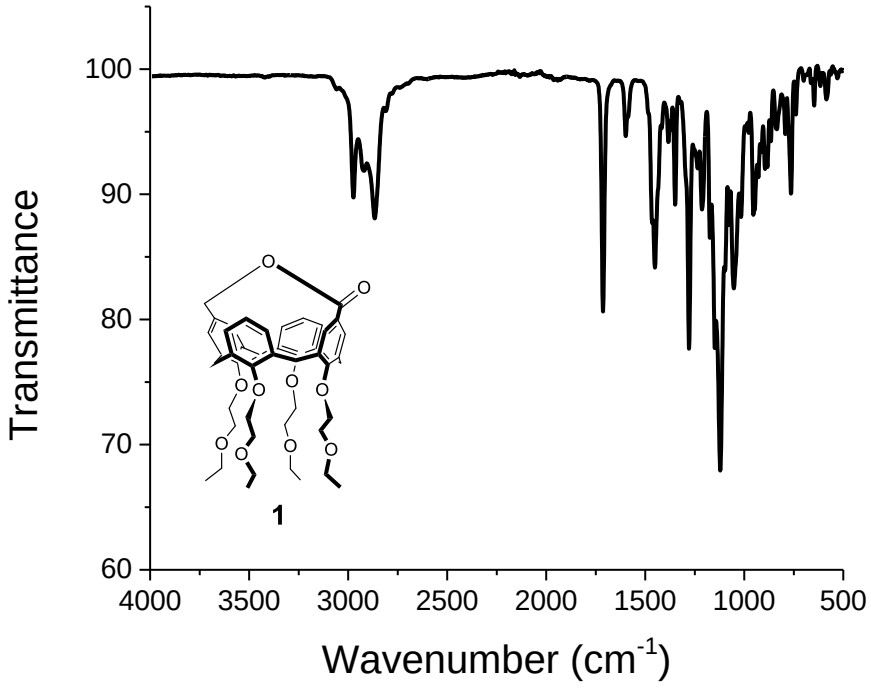

Figure S22. FT-IR spectrum of lactone **1**.

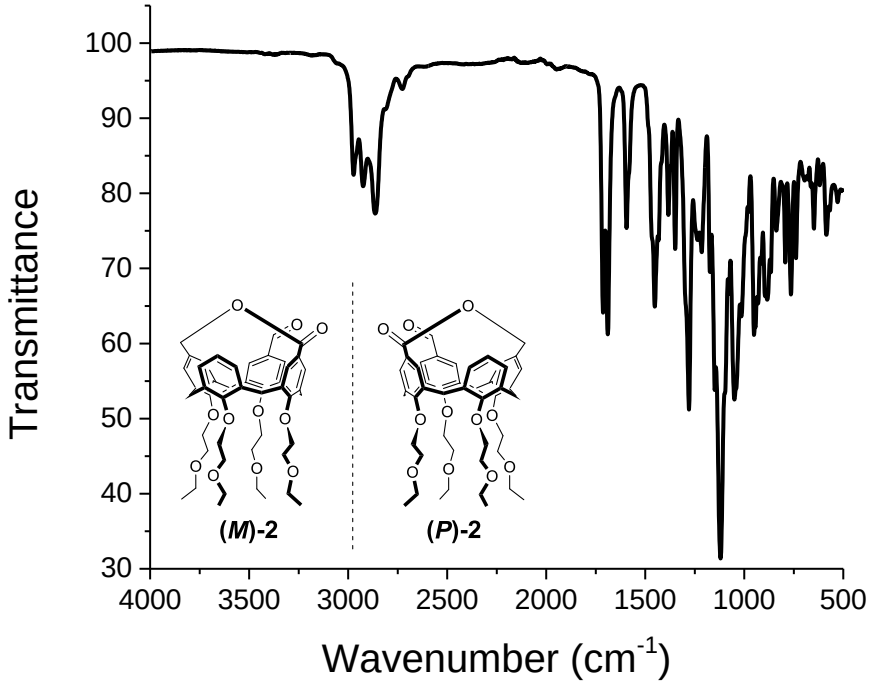

Figure S23. FT-IR spectrum of lactone **2**.

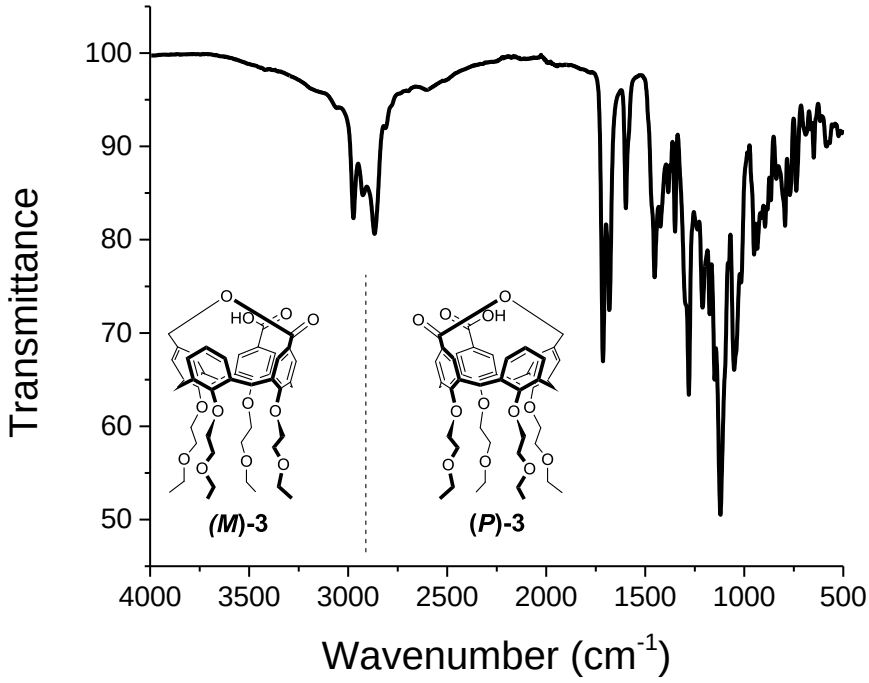

Figure S24. FT-IR spectrum of lactone **3**.

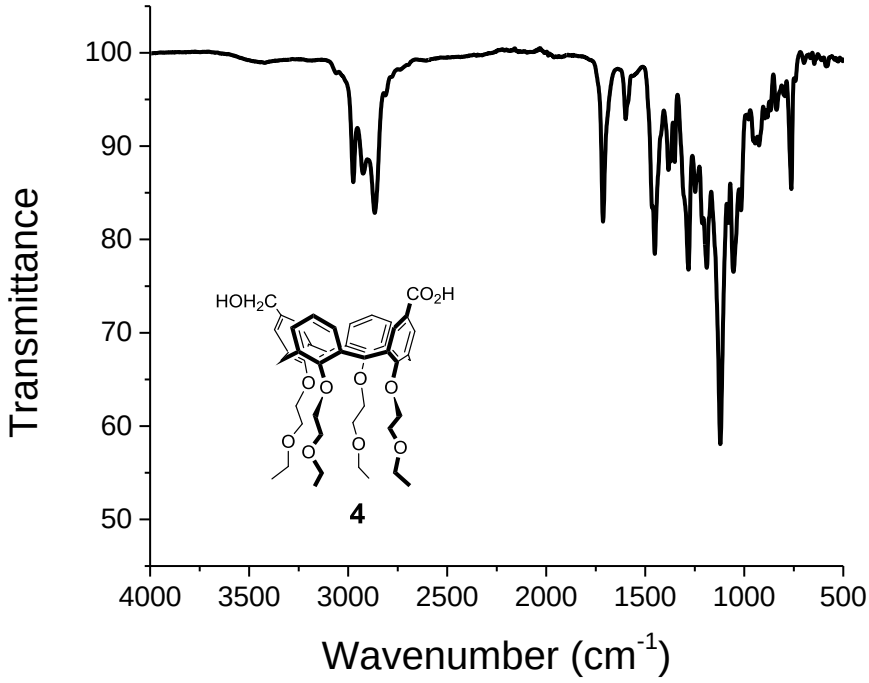

Figure S25. FT-IR spectrum of compound **4**.

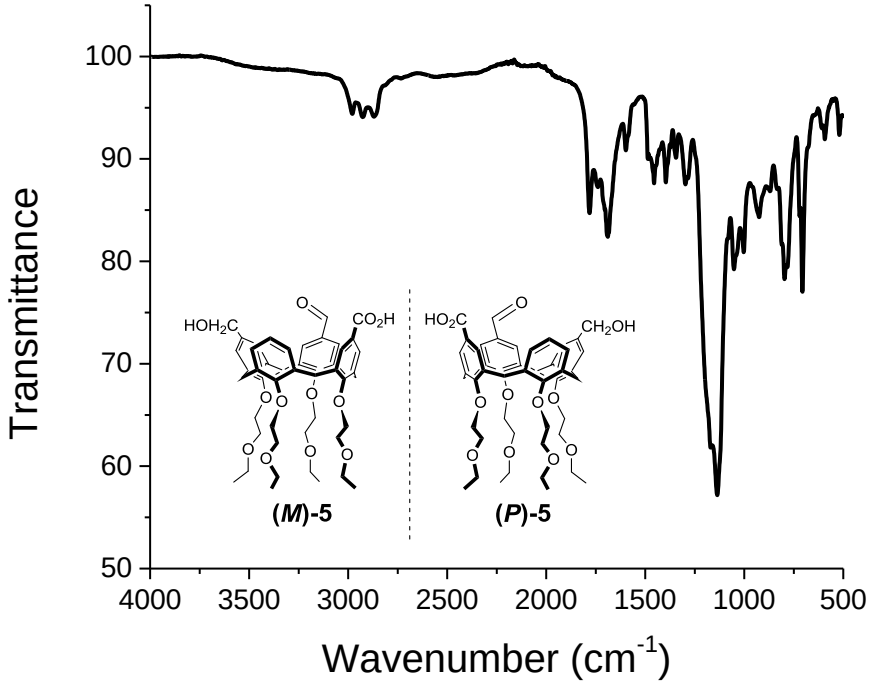

Figure S26. FT-IR spectrum of compound **5**.

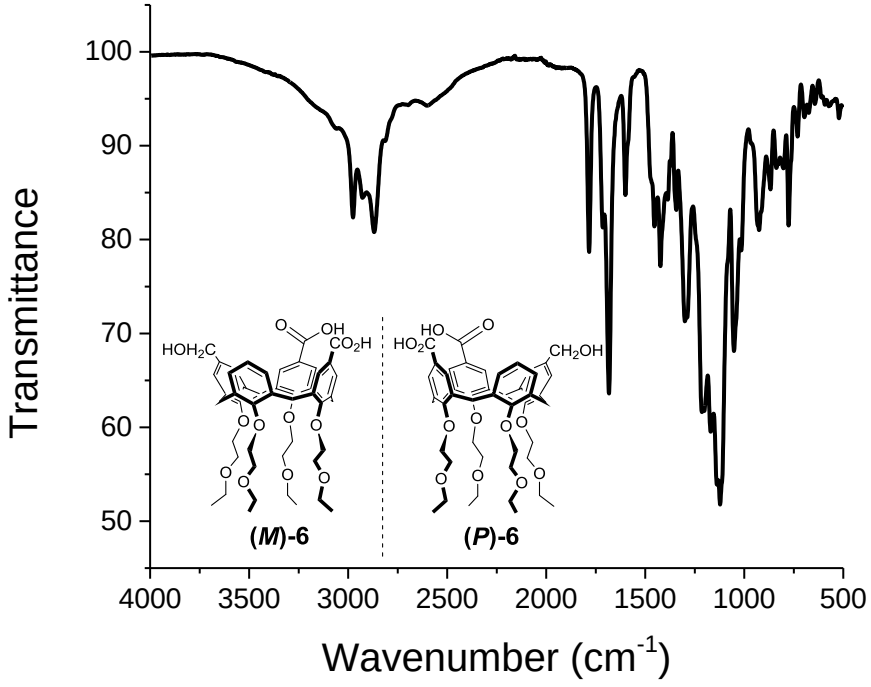

Figure S27. FT-IR spectrum of compound **6**.

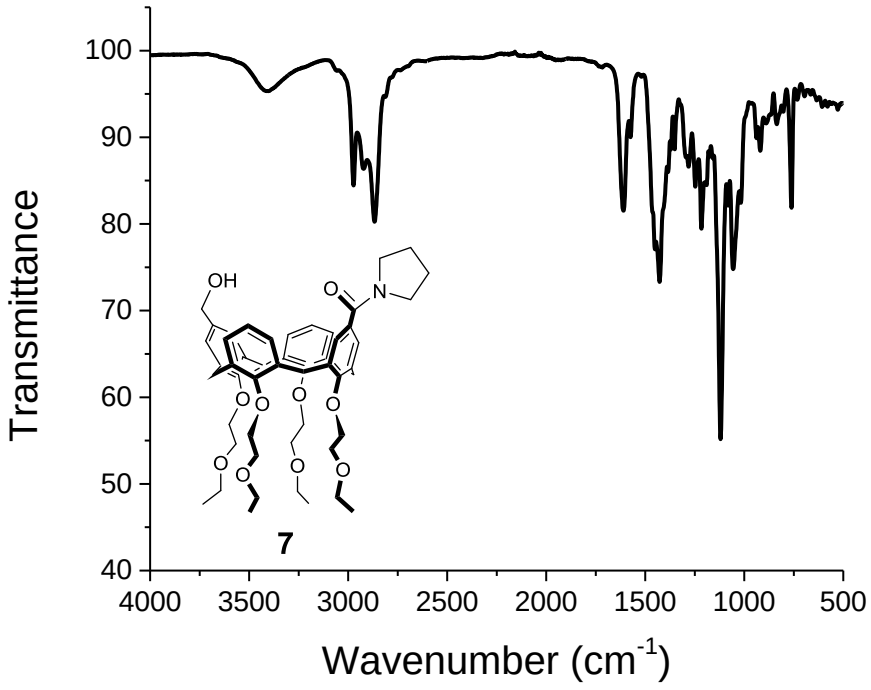

Figure S28. FT-IR spectrum of compound **7**.

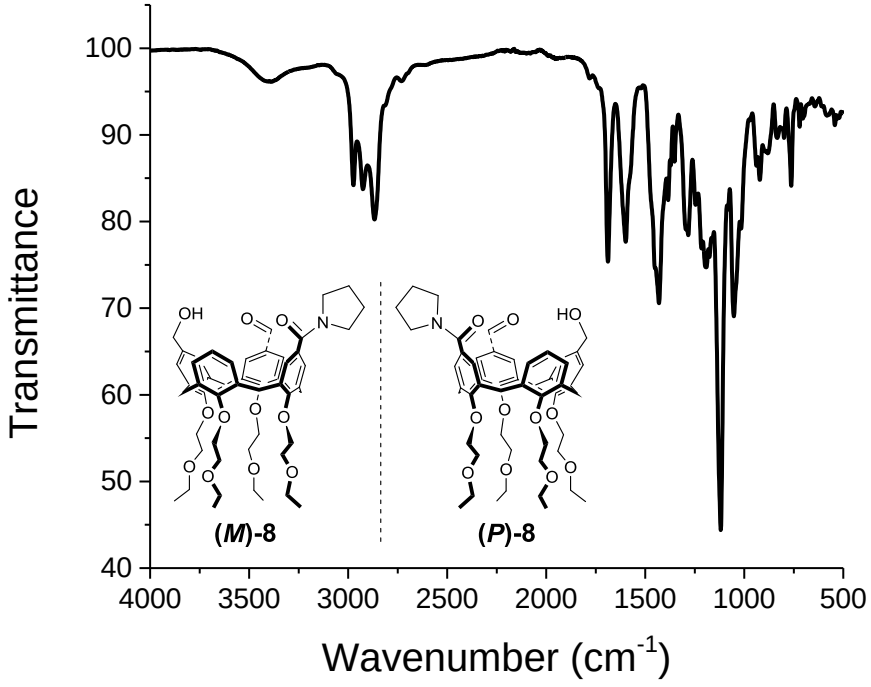

Figure S29. FT-IR spectrum of compound **8**.

IR spectra comparisons

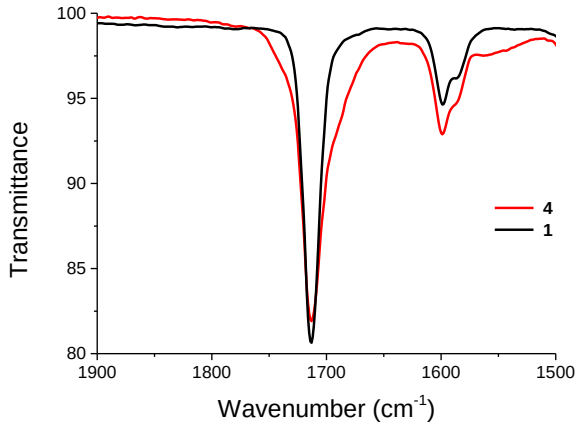

Figure S30. Comparison of the carbonyl region of the FT-IR spectra of **1** (black line) and its precursor **4** (red line).

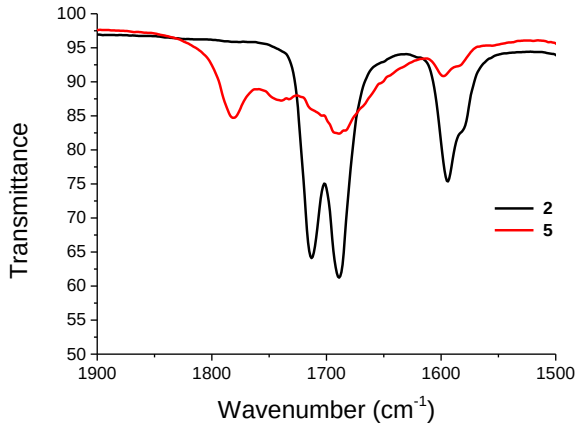

Figure S31. Comparison of the carbonyl region of the FT-IR spectra of **2** (black line) and its precursor **5** (red line).

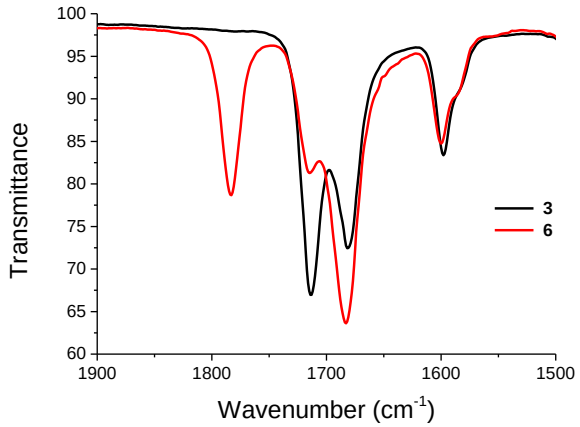

Figure S32. Comparison of the carbonyl region of the FT-IR spectra of **3** (black line) and its precursor **6** (red line).

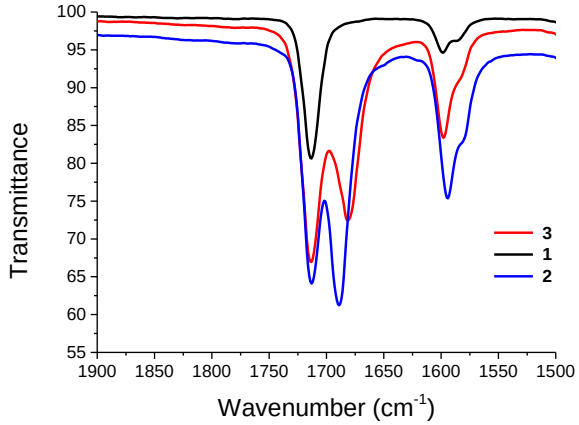

Figure S33. Comparison of the carbonyl region of the FT-IR spectra of **1** (black line), **2** (blue line), and **3** (red line).

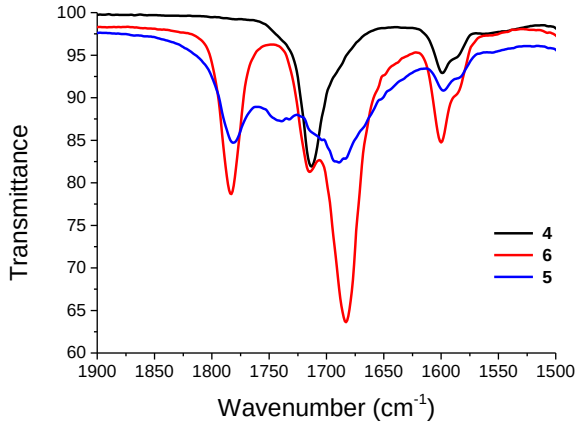

Figure S34. Comparison of the carbonyl region of the FT-IR spectra of **4** (black line), **5** (blue line), and **6** (red line).

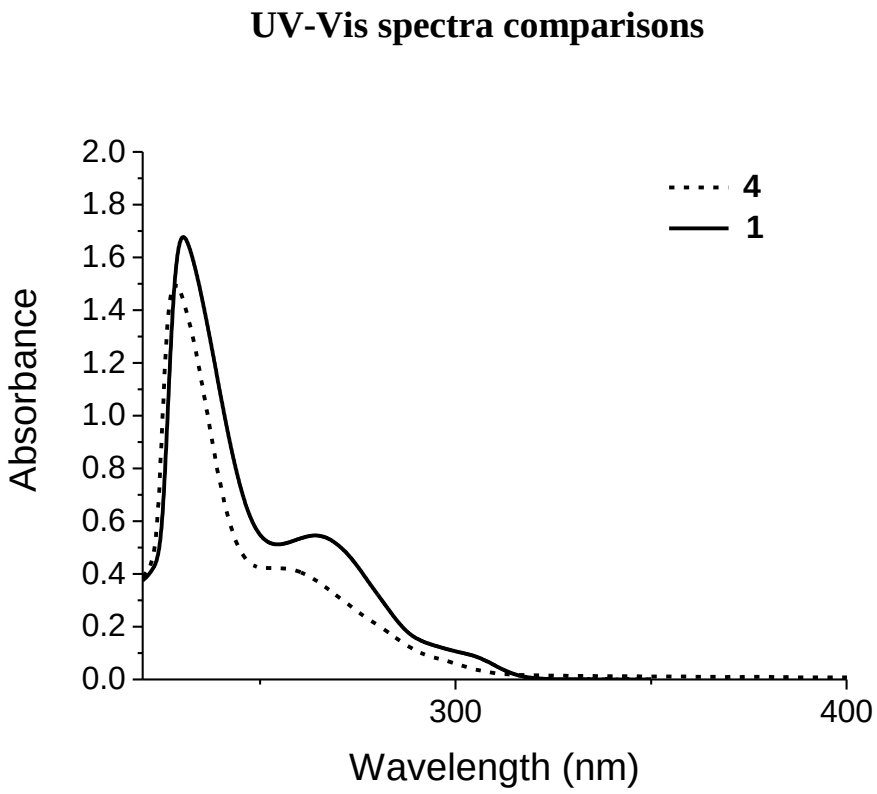

Figure S35. Comparison of UV-vis spectra ($CHCl_3$, 298 K, 1 cm optical path) of **1** (solid line) and **4** (dashed line).

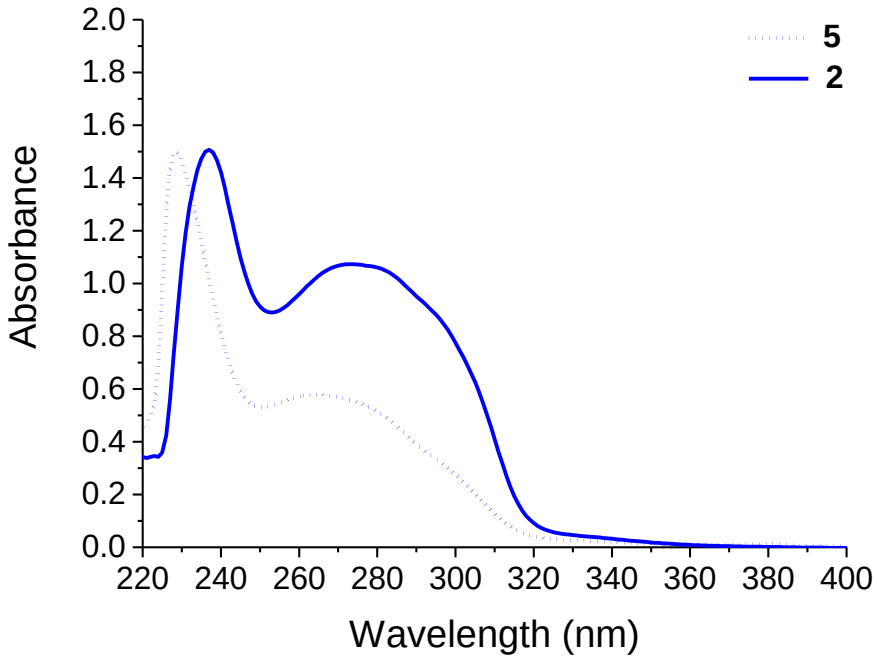

Figure S36. Comparison of UV-vis spectra ($CHCl_3$, 298 K, 1 cm optical path) of **2** (solid line) and **5** (dashed line).

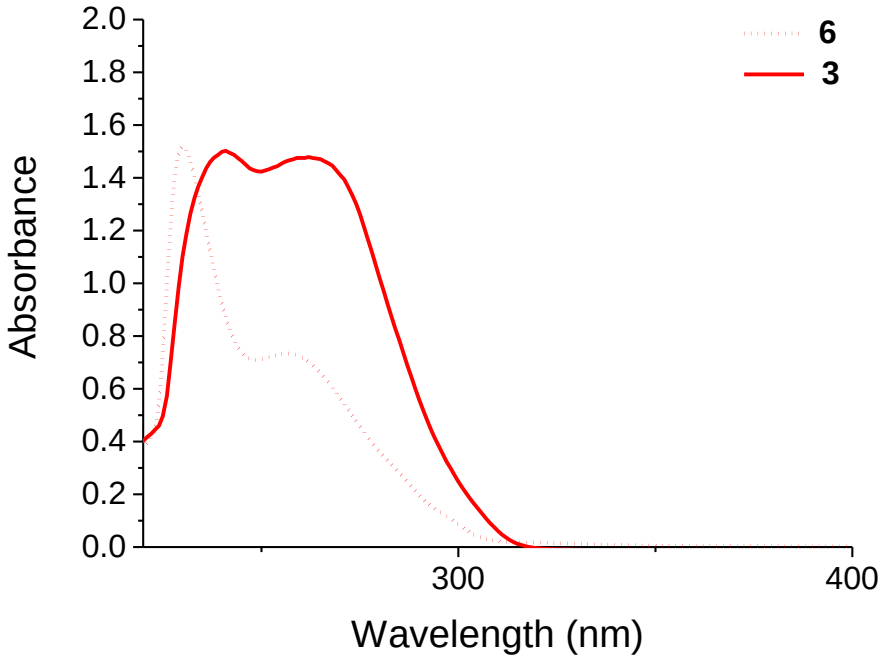

Figure S37. Comparison of UV-vis spectra ($CHCl_3$, 298 K, 1 cm optical path) of **3** (solid line) and **6** (dashed line).

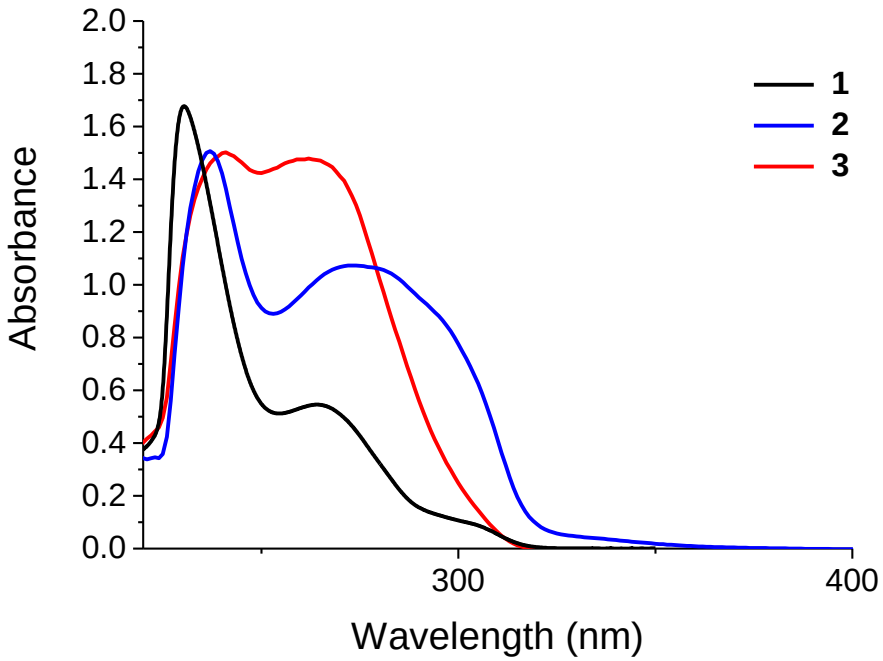

Figure S38. Comparison of UV-vis spectra ($CHCl_3$, 298 K, 1 cm optical path) of **1** (black line), **2** (blue line), and **3** (red line).

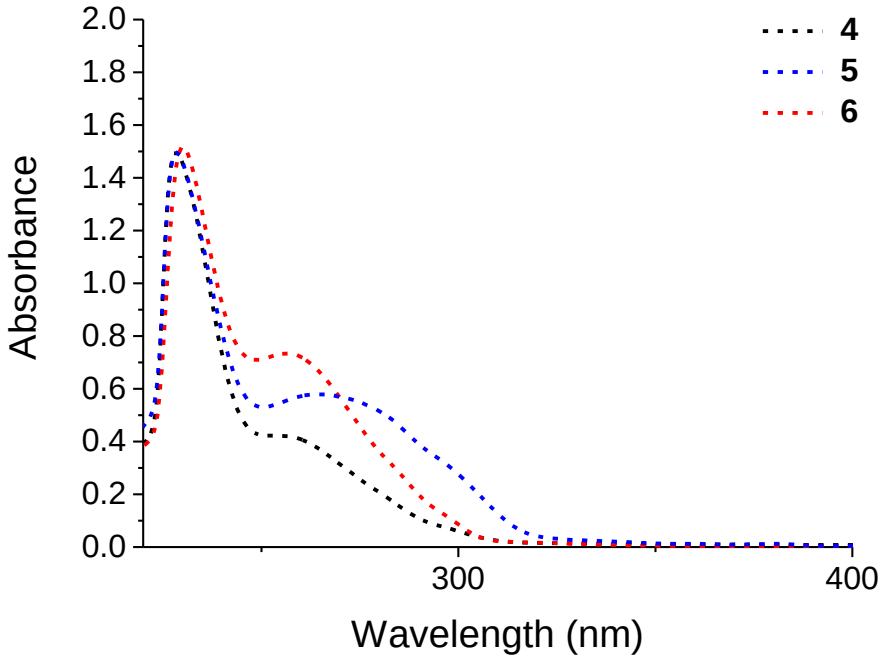

Figure S39. Comparison of UV-vis spectra ($CHCl_3$, 298 K, 1 cm optical path) of **4** (black line), **5** (blue line), and **6** (red line).

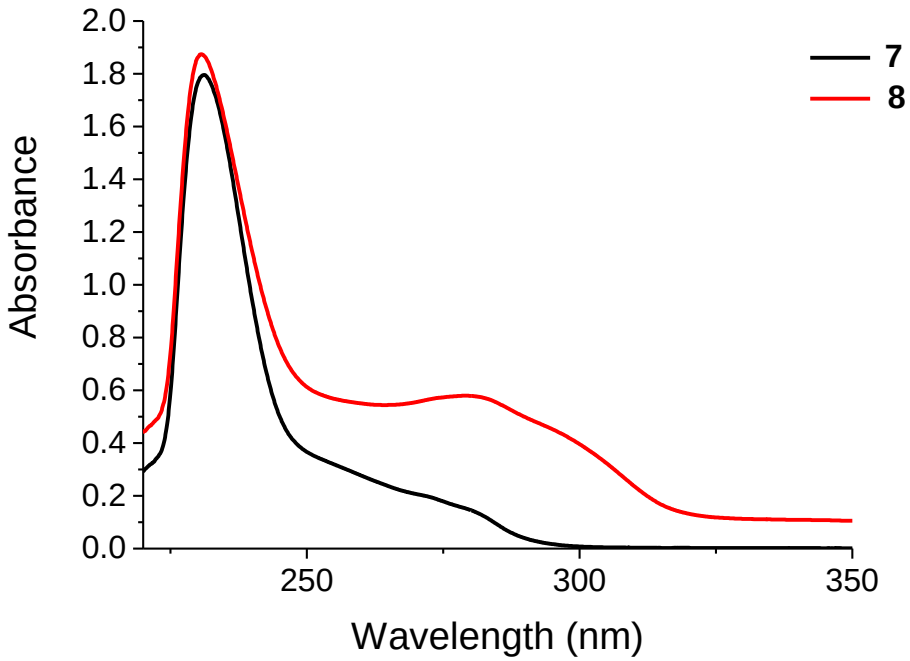

Figure S40. Comparison of UV-vis spectra ($CHCl_3$, 298 K, 1 cm optical path) of **7** (black line), and **8** (red line).

GPC separations

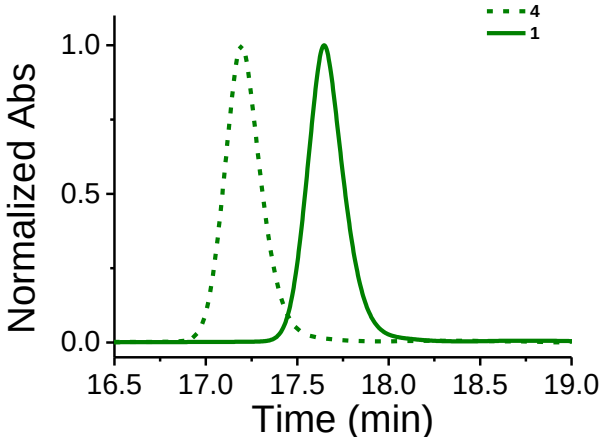

Figure S41. GPC chromatograms of lactone **1** (solid line) and its precursor **4** (dashed line).

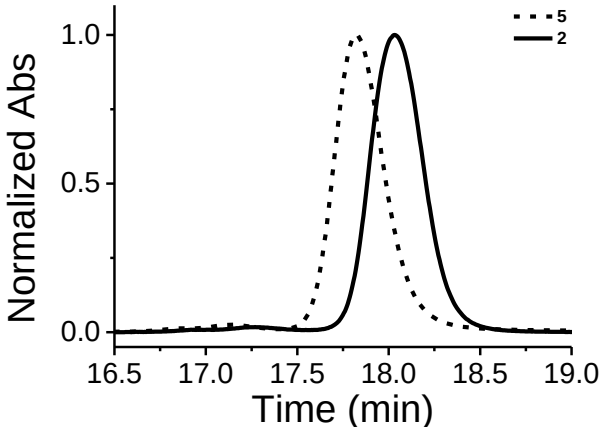

Figure S42. GPC chromatograms of lactone **2** (solid line) and its precursor **5** (dashed line).

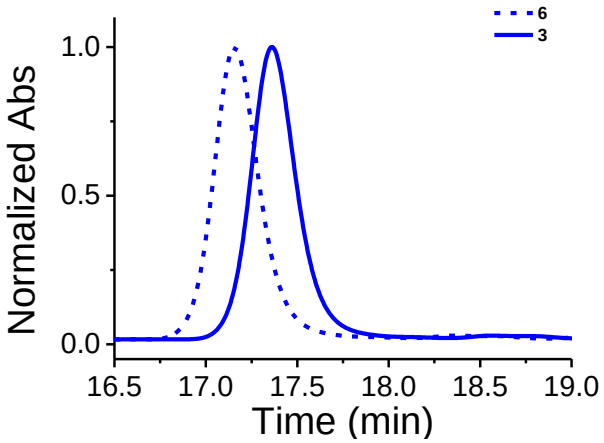

Figure S43. GPC chromatograms of lactone **3** (solid line) and its precursor **6** (dashed line).

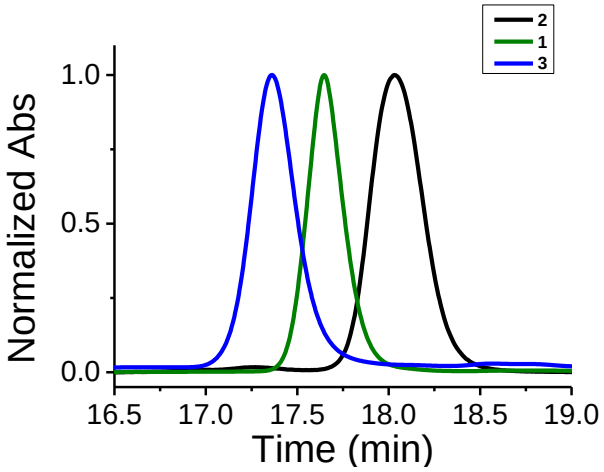

Figure S44. GPC chromatograms of lactones **1** (green line), **2** (black line), and **3** (blue line).

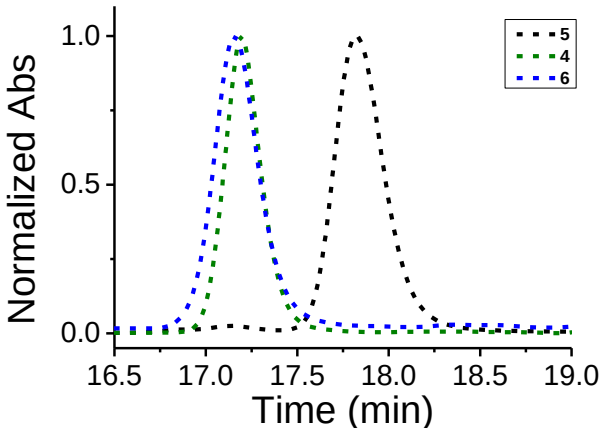

Figure S45. GPC chromatograms of compounds **4** (green line), **5** (black line), and **6** (blue line).

Chiral HPLC separations

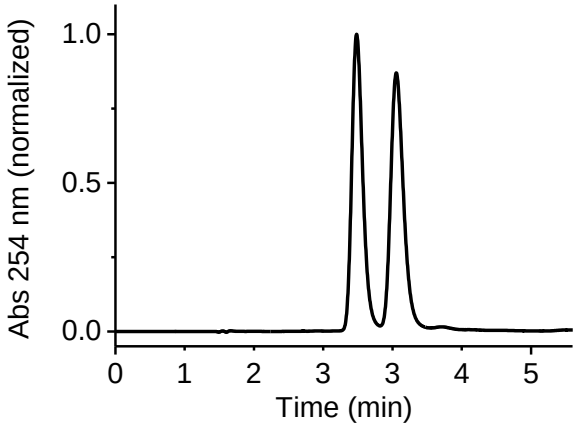

Figure S46. Chiral HPLC separation (85:15 Hex/IPA, 298 K, flow rate 0.2 mLmin) of lactone **2.**

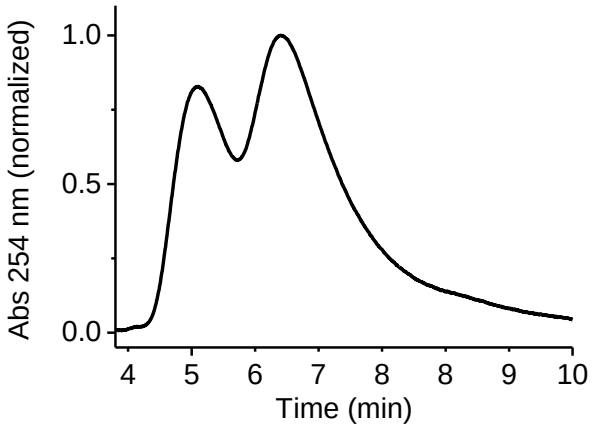

Figure S47. Attempt at performing the chiral HPLC separation (85:15 Hex/IPA, 298 K, flow rate 0.2 mLmin) of **5.**

.

^{1}H NMR of racemic lactone 2 in the presence of (R)-(−)-1-(9-Anthryl)-2,2,2-trifluoroethanol

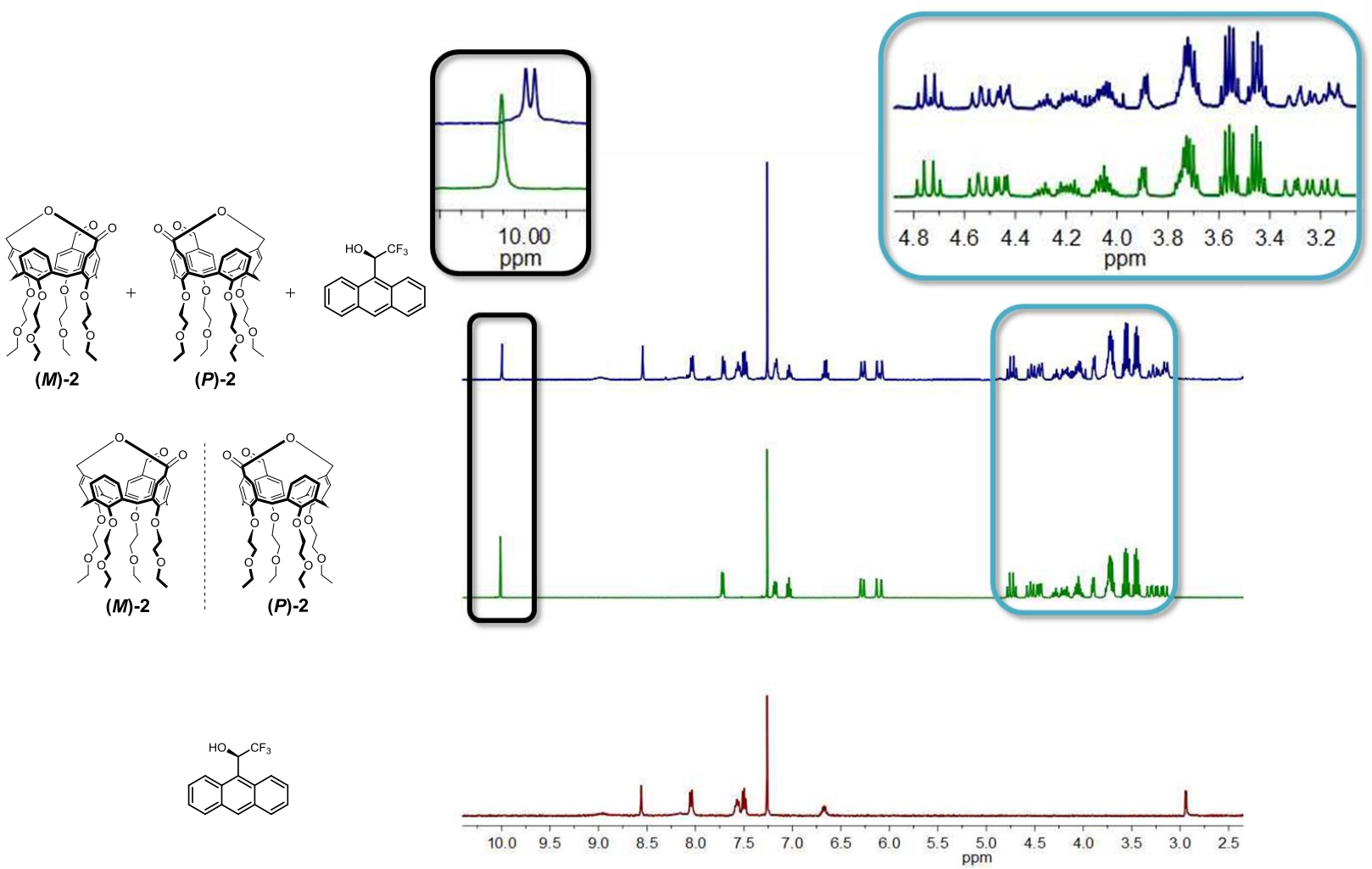

Figure S48. Comparison of ^{1}H NMR spectra of (R)-(−)-1-(9-Anthryl)-2,2,2-trifluoroethanol, 2, and 2 + (R)-(−)-1-(9-Anthryl)-2,2,2-trifluoroethanol in $CDCl_3$.

Computational section

All calculations were performed utilizing Gaussian 09W.[S1] In order to simplify the calculations, the ethylene glycol tails of compounds **1-8** were truncated to simple $–OCH_3$ substituents on the lower ring to generate a set of related compounds **I-VIII**. Initial input geometries were generated from a crystal structure of calix[4]arene, with conformers being generated by hand, and ranged from 4-8 chemically reasonable geometric each of isomers of **I-VIII**. Lower energy or interesting structural geometries were determined at a RB3LYP/3-21G level of theory, with final geometry optimization using the RB3LYP[S2,S3] methodology and the 6-13G** basis set.[S4] This functional and basis set combination has already been shown to accurately reproduce key structural and NMR features for a series of loosely related calix-4-arenes. All[S5] reported geometries contained no negative frequencies.

NMR tensors for atoms were determined via geometry reoptimization of low energy conformers (below +4 kcal/mol for observed energy minimum) at the RB3LYP/6-31G** level of theory using a polarized continuum model (PCM) using the integral equation formalism variant[S6] with $CHCl_3$ as the solvent environment. These optimized structures were then used to calculate the NMR shielding tensors using the gauge-independent atomic orbital (GIAO) method.[S7] The calculated shielding tensors were then referenced to TMS optimized and calculated at the same level of theory. Compounds with multiple low energy conformers have their chemical shifts reported as a average of the Boltzmann weighted distribution of these conformers at room temperature.

Structures were visualized with Gaussview 09.

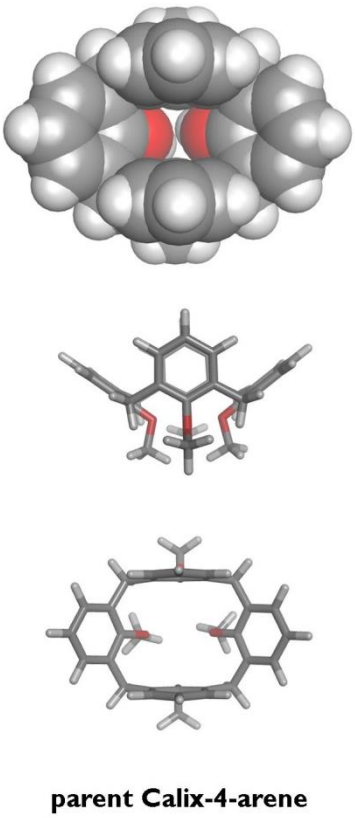

Figure S49. Representative view of lowest energy conformers of **parent calix-4-arene.**

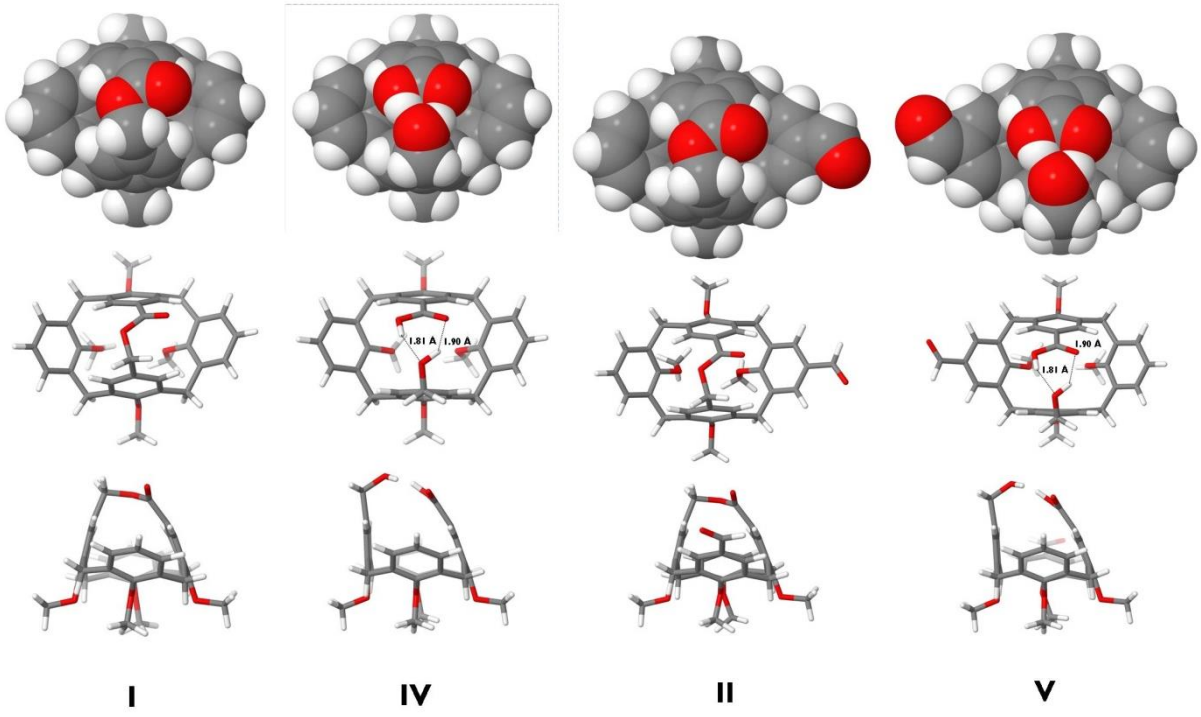

Figure S50. Representative view of lowest energy conformers of compounds **1** (**I**, left), **4** (**IV**, middle-left), **2** (**II**, middle-right) and **5** (**V**, right)

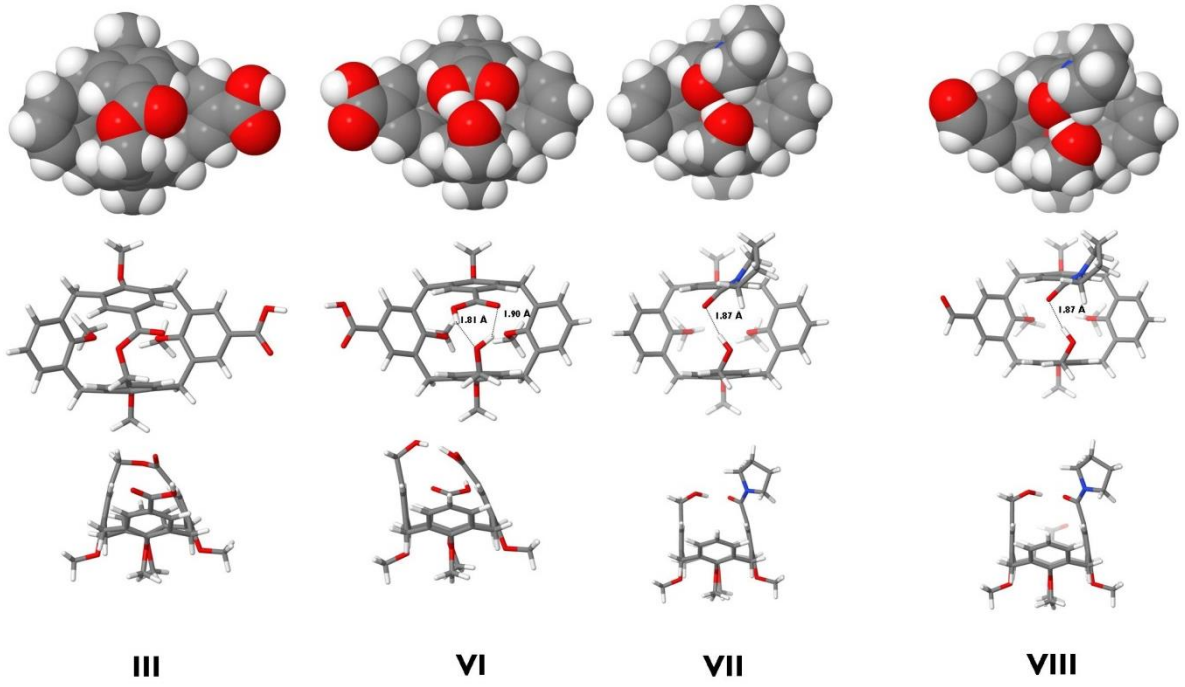

Figure S51. Representative view of lowest energy conformers of compounds **3** (**III**, left) and **6** (**VI**, middle-left), 7 (**VII**, middle-right) and **8** (**VIII**, right).

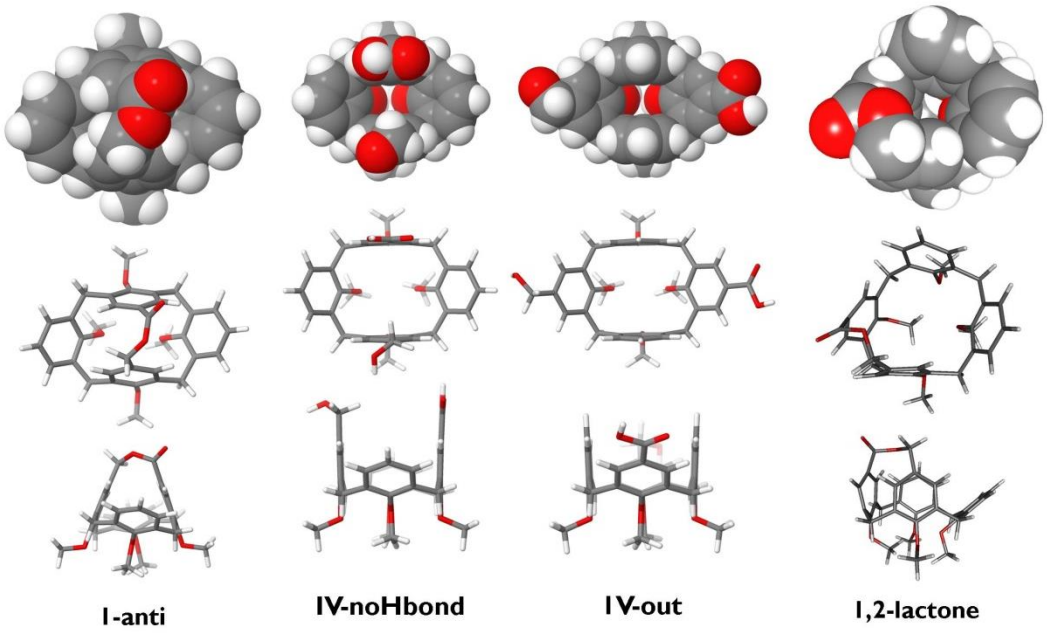

Figure S52. Representative views of higher energy conformers of compound **1** an anti-lactone conformation (**I-anti**), **4** with a broken H-bond network (**IV-noHbond**, middle left), substituents on distal rings (**IV-out**, middle right), and a regioisomer of **1** with the lactone formed across the 1,2 rings (**1,2-lactone**, right).

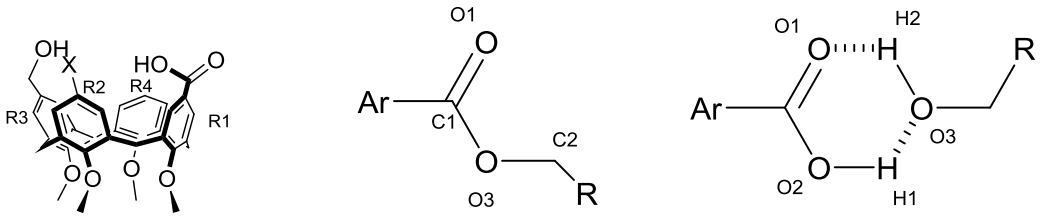

Figure S53. Numbering convention used for rings (middle, structure **IV** with R=H), bond lengths and bond angles about the formed lactone ring (middle, compounds **1**–**3**) or the H-bond network (right, compounds **4**–**8**)

Table S1. Energetic and structural analysis of all calculated structures

Structure	B3LYP Energy (hartrees)	ΔH (kcal/mol)	Ring distance(Å)[a]		Lactone Lengths (Å)[b]				Lactone Bond Angles (deg)[b]	
			Ring 1-3	Ring 2-4	C_1-O_1		C_1-O_3		C_{Ar}-C_1-O_3	O_1-C_1-O_3-C_2
calix-4-arene	-1539.567688		5.54	9.91						
I	-1766.226659	0.00[c]	3.69	10.29	1.214		1.369		112.54	-44.32
I-anti	-1766.2118	9.32[c]	3.28	10.39	1.209		1.365		121.78	167.81
1,2-lactone	-1766.16177118	40.7[c]			1.210		1.380		109.84	52.48
II	-1879.552597		3.69	10.31	1.214		1.368		112.53	-43.79
III	-1954.804905		3.69	10.3	1.214		1.369		112.54	-44.21
					H-Bond Lengths (Å)[b]				H-Bond Angles (deg)[b]	
					O_1-O_3	O_1-H_2	O_2-O_3	O_3-H_1	O_1-H_2-O3	O_2-H_1-O_3
IV	-1842.679796	0.00[d]	4.50	10.18	2.73	1.90	2.71	1.81	141.10	149.90
IV-noHbond	-1842.674867	3.09[d]	5.49	9.91	6.70	7.55	6.36	6.45		
IV-out	-1842.674879	3.09[d]	9.91	5.58	13.7	14.1	13.9	14.6		
V	-1956.00636		4.5	10.18	2.73	1.90	2.71	1.81	141.44	150.04
VI	-2031.258595		4.5	10.18	2.73	1.90	2.71	1.81	140.85	150.06
VII	-1978.855301		4.85	10.07	2.83	1.87			167.56	
VIII	-2092.181594		4.86	10.07	2.83	1.87			167.94	

[a]Distance between rings in the calixarerne structure are reported as inter-atomic distances between apical carbons on rings **1** (benzoic acid) and **3** (benzyl alcohol), or between apical carbons on ring **2** (with R group = H, COOH, or COH) and ring **3** (R group = H), [b] for numbering of atoms within this table, please see Figure S51 above, [c] Energy referenced to structure I, [d] Energy reference to structure IV

Table S2. Bond angles of methylene bridges around the calix-4-arene framework

Structure	Bond Angles (deg)[a]				Analysis		
	R1-CH_2-R2	R2-CH_2-R3	R3-CH_2-R4	R4-CH_2-R1	Average	Variance	Spread
calix-4-arene	111.69	111.74	111.71	111.74	111.72	0.00	0.05
I	109.28	112.86	110.11	111.21	110.87	1.80	3.58
I-anti	108.84	111.95	108.70	112.63	110.53	3.16	3.93
II	109.28	112.87	110.09	111.18	110.86	1.81	3.59
III	109.25	112.81	110.10	111.15	110.83	1.76	3.56
IV	109.53	112.73	113.50	109.91	111.42	2.97	3.97
IV-noHbond	111.57	111.68	111.59	111.61	111.61	0.00	0.11
IV-out	111.86	111.48	111.47	111.86	111.67	0.04	0.39
V	109.88	113.73	112.58	109.36	111.39	3.32	4.37
VI	109.91	113.46	112.74	109.41	111.38	2.77	3.33
VII	110.49	112.36	111.44	111.02	111.33	0.47	1.87
VIII	111.32	111.51	112.25	110.20	111.32	0.54	2.05

[a] for numbering of atoms within this table, please see Figure S51 above.

Table S3. Energetic analysis for conformers of **I**, and **IV** in $CHCl_3$

Structure	B3LYP Energy	differences (kcal/mol)	# of accessible structures	Boltzmann weighting	Distribution (%)
I	-1766.236666	0.00	--	--	--
I-anti	-1766.223398	8.33[a]	--	--	--
IV	-1842.689342	0.00[b]	2	2	0.567023
IV-noHbond	-1842.687915	0.90[b]	4	0.88	0.24966
IV-out	-1842.687623	1.08[b]	4	0.65	0.183317

[a]Relative to structure **I** [b] Structures more than 8kcal/mol away from the ground state were not considered for the NMR calculation [c]Relative to structure **IV**

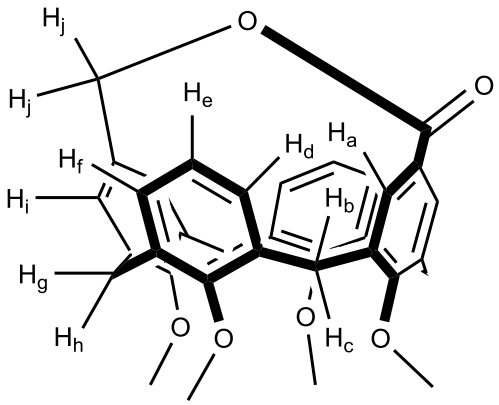

Figure S54. Schematic for the assignment of protons in the calculated spectra.

Table S4. Observed and calculated NMR chemical shifts for compounds **1**, **4**, **I**, **IV**, and **I-anti**.[a]

Proton	I[a]	IV[a]	I-anti[a]	I (corr)[b]	1 exp[c]	IV (corr)[b]	4 exp[c]	I-anti (corr)[b]	Δ 4 to 1 (exp)[c]	Δ IV to I[b]	Δ IV to I-anti[b]
H_a	24.85	24.24	25.41	7.12	6.27	7.73	7.15	6.55	-0.88	-0.61	1.17
H_b	28.75	28.56	28.67	3.22	--[d]	3.40	--[d]	3.29		-0.18	0.11
H_c	27.17	27.18	27.15	4.80	4.50	4.78	4.50	4.82	0.00	0.02	-0.04
H_d	24.46	24.54	24.39	7.50	7.15	7.42	6.90	7.57	0.25	0.08	-0.15
H_e	24.60	24.72	24.56	7.36	7.00	7.25	6.70	7.41	0.30	0.11	-0.16
H_f	24.48	24.55	24.41	7.49	7.15	7.41	6.80	7.56	0.35	0.08	-0.14
H_g	28.79	28.67	28.68	3.18	--[d]	3.29	--[d]	3.29		-0.11	0.01
H_h	27.18	27.22	27.12	4.78	4.50	4.74	4.50	4.84	0.00	0.04	-0.10
H_i	25.18	24.73	25.76	6.79	6.10	7.24	6.35	6.20	-0.25	-0.45	1.04
H_j	26.96	27.34	26.90	5.00	4.75	4.62	3.90	5.06	0.85	0.38	-0.44

[a]NMR shielding tensor (σ) as calculated at the RB3LYP/6-31G** level of theory with PCM solvation in $CHCl_3$ and Boltzmann weighting of conformers, [b]ppm relative to TMS calculated in $CHCl_3$ at the same level of theory (δ_{calc}), [c]ppm as observed in $CDCl_3$ NMR (δ_{exp}), [d] experimental assignment not possible with confidence, due to superimposition with other signals.

Calixarene lactones π* antibonding orbital

The accessibility of the reactive π* antibonding orbital of the lactone is relatively hindered for larger nucleophiles. As shown in Figure S55, larger nucleophiles can only approach the lactone from outside the calixarene, while smaller nucleophiles (like water) could approach from either outside or within the calix[4]arene cavity.

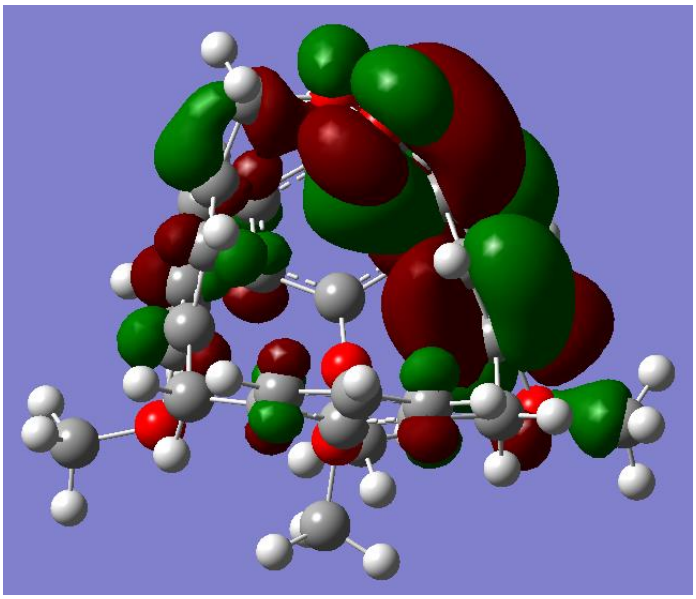

Figure S55. LUMO density plot of the calix-4-arene lactone **1**. As can be seen from the plot, the antibonding orbitals around the lactone are only approachable by larger nucleophiles from the outside of the cavity. Calculations performed at the B3LYP/6-31G** level of theory.

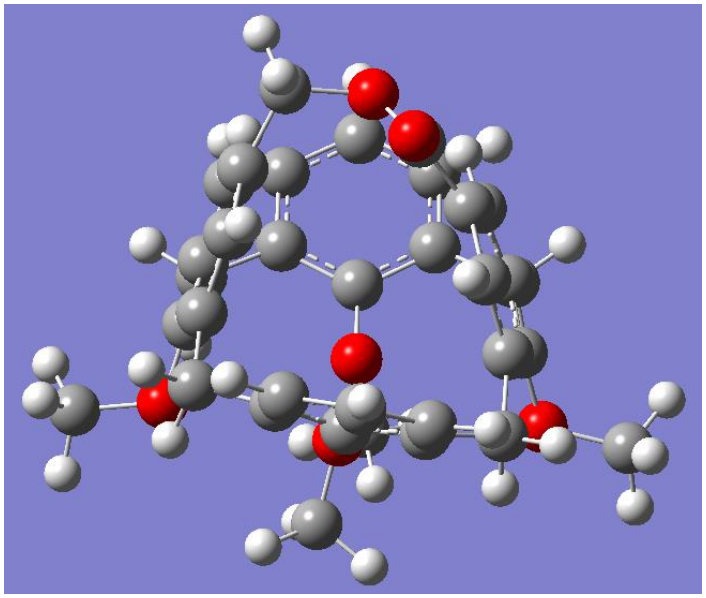

Figure S56. Atomistic representation of **1** for comparison to the LUMO overlay plot in Figure S55.

References

S1) M. J. Frisch, G. W. Trucks, H. B. Schlegel, G. E. Scuseria, M. A. Robb, J. R. Cheeseman, G. Scalmani, V. Barone, G. A. Petersson, H. Nakatsuji, X. Li, M. Caricato, A. Marenich, J. Bloino, B. G. Janesko, R. Gomperts, B. Mennucci, H. P. Hratchian, J. V. Ortiz, A. F. Izmaylov, J. L. Sonnenberg, D. Williams-Young, F. Ding, F. Lipparini, F. Egidi, J. Goings, B. Peng, A. Petrone, T. Henderson, D. Ranasinghe, V. G. Zakrzewski, J. Gao, N. Rega, G. Zheng, W. Liang, M. Hada, M. Ehara, K. Toyota, R. Fukuda, J. Hasegawa, M. Ishida, T. Nakajima, Y. Honda, O. Kitao, H. Nakai, T. Vreven, K. Throssell, J. A. Montgomery, Jr., J. E. Peralta, F. Ogliaro, M. Bearpark, J. J. Heyd, E. Brothers, K. N. Kudin, V. N. Staroverov, T. Keith, R. Kobayashi, J. Normand, K. Raghavachari, A. Rendell, J. C. Burant, S. S. Iyengar, J. Tomasi, M. Cossi, J. M. Millam, M. Klene, C. Adamo, R. Cammi, J. W. Ochterski, R. L. Martin, K. Morokuma, O. Farkas, J. B. Foresman and D. J. Fox, *Gaussian 09, Revision A.02*, Gaussian, Inc., Wallingford CT, 2016.

S2) A. D. Becke, *J. Chem. Phys.* 1993, **98,** 5648–5652.

S3) P. J. Stephens, F. J. Devlin, C. F. Chabalowski and M. Frisch, *J. Phys. Chem.* 1994, **98**, 11623–11627.

S4) W. J. Hehre, R. Ditchfield and J. A. Pople, *J. Chem. Phys.* 1972, **56**, 2257–2261.

S5) R. N. Guzzo, M. J. Cunha Rezende, V. Kartnaller, W. de M. Carneiro, S. R. Stoyanov and L. Moreira da Costa, *J. Mol. Struct.* **2018**, *1157*, 97–105.

S6) J. Tomasi, B. Mennucci and R. Cammi, *Chem. Rev.* 2005, **105**, 2999-3093.

S7) J. R. Cheeseman, G. W. Trucks, T. A. Keith and M. J. Frisch, *J. Chem. Phys.* 1998, **104**, 5497.